UNIVERSIDAD DE CONCEPCIÓN
FACULTAD DE CIENCIAS FÍSICAS Y MATEMÁTICAS

MORPHOLOGICAL STUDY OF LEAD HALIDE PEROVSKITES CAST AT DIFFERENT SPIN VELOCITIES

Applying dynamic scaling theory for a synthesis process with no deposition time

Por: Camilo Fernando Alegría Núñez

Tesis presentada a la Facultad de Ciencias Físicas y Matemáticas de la Universidad de Concepción para optar al grado académico de Magíster en Ciencias con Mención en Física

Abril 2024
Concepción, Chile

Profesor Guía: Noelia Benito

A mi hermano Antonio

AGRADECIMIENTOS

Este trabajo fue posible gracias a la beca ANID Magíster Nacional número 22231713 y el proyecto ANID FONDECYT 11180837.
Agredecer a la Universidad de Concepción, especialmente a la facultad de Ciencias Físicas y Matemáticas por la formación, espacio y apoyo durante el proceso de magister, inclyendo al conjunto de funcionarios que me permitieron trabajar de sol a sol en las dependencias de la facultad.
A la Dra. Noelia Benito, su guía y mentoria son invaluables para mí, mostrandome cómo avanzar a través de discusiones y sugerencias, esclareciendo dudas y fomentando ideas. Muchas, muchas gracias.
Al Dr. Julio Oliva, mi infinita gratitud por su apoyo, preocupación, su cercania y aprecio.
A mi compañera de laboratorio, Arelly, quien me impulsó y alentó durante las jornadas de trabajo, empujándome a postular a cursos que nos llevaron del otro lado del Atlántico, continuamente invitándome a seguir la vía investigativa.
A mis amigos Samuel y Nicolás, sin los cuales no hubiese explorado la vida de laboratorio y con quienes mi intuición científica se nutrió mediante multiples y extensas conversaciones.
Ayleen y Francisco, quienes en su infinita paciencia me permetieron trabajar con ellos mientras aún estaba en el proceso de redacción, trabajo que sustentó económicamente el último trecho de esta tesis.
Amigos como Scarlett y Marcel son los que debiesen tener todos. Un corazón apretado recuerda su presencia inmediata, sonrisas, música y apoyo mutuo. Haciendo patria los veo por las redes, que siga así.
Nico Cáceres, Aníbal Luciano y Jota, simepre ansío el próximo encuentro, la próxima broma y juego verbal en algún café de esta tierra. Sepan que cuando más gris se ve el cielo es cuando recuerdo nuestros ires y venires, y me invitan a seguir.
A Moyarzo por siempre estar dispuesto a entretener mis dudas, por esa forma tan apasionada de pensar en la física y por las horas de música que pasaron y por las que nos aguardan. Igualmente a Anibal Neira por acompañarme a mi y a Monse, dilucidando entre todos que es esto de crecer y vivir.
Familia querida, Pachi, Kelo y Tinin, nada podría haber hecho sin ustedes. Poco

pueden hacer las palabras que un abrazo no pueda plasmar. Los amo.
Mi amor, Monserrat. Esta tesis no fue el único desarollo nuevo en mi vida, también empezamos la construcción de nuestra vida juntos a la par que se construía este documento. Tus hombros son el acogedor cimiento que me mantuvo de pie en los momentos bajos, y tu sonrisa la coronación de cada pequeña victoria. Te amo de forma incalculable.

Abstract

The present work centers on the use of dynamic scaling theory when dealing with processes which do not depend on deposition times. Our hypothesis is that through film thickness one can successfully calculate the critical exponents of a system, classifying it and understanding the role that the controlled variable dominating the material dispersion process has on structure formation. This hypothesis was tested by studying the effects of spin velocity on film morphology for lead halide perovskite, synthesized by way of spin-coating, setting different top speeds at 600, 700, 800, 900, 1000, 1500 and 2000[RPM]. The first part of the document deals with the theory of semiconductors in order to understand what type of material we are working with and the characterization method of X-ray diffraction. Then, a chapter is dedicated to dynamic scaling theory which is the base of our statistical analysis and the main part of our hypothesis, since is how we calculate the critical exponents. Finally, the results obtained from X-ray diffraction, sample imaging, statistical analysis of the films and computed critical exponents are shown in the fifth chapter, where we compare the use of different statistical tools, specifically the auto-correlation function, heigh-height correlation function and the software WSXM. When it comes to the specific characterization techniques, tetragonal phase perovskite fabrication was confirmed thanks to X-ray diffraction, with the spin velocity having an slight effect on crystallite size. Atomic force microscopy was used for sample imaging and profilometry, done at our laboratory, with the statistical analysis of height distribution done using dynamic scaling theory. We successfully obtained exponents which correspond to a one dimensional KPZ system, proving our hypothesis correct when it comes to the use of thickness instead of time for dynamic scaling analysis.

Keywords – Perovskite, Solar cells, Lead halide, Spin casting, Morphology, Dynamic

Contents

List of Tables

List of Figures

Chapter 1

Introduction

1.1 Preface

Solid state physics and material science have been the backbone of technological development since the invention of the transistor leading to the explosion of technology we are still living under, some calling it a second industrial revolution. We have uncountable uses for the fascinating phenomena found in the mesoscale, from computing devices to energy harvesting, the limit seems to always be the available knowledge at the time and, more crucially, our imagination. As science progressed so did what we were capable of conceiving, look no further than the creation of the computer. From being the size of a whole room to the mobile cellphone, they were molded by the understanding of an special type of materials: semiconductors, and all of these is because of their special capabilities. The characteristics that make them the corner stone of these technological advancements are the phototelectric effect Einstein (1905) and band structure Bloch (1928). Both of these opened the use of these materials to other fields such as energy production, making their appearance as the first solar cells and subsequently the firsts solar panels. For this reason they have become crucial once again since we currently are going through a climate crisis, with the main negative contributors being the use of fossil fuels for energy, hence, renewable energy sources such as solar are at the forefront of our efforts to combat anthropogenic climate change.

This creates a need for technical advance in the areas of material science since a better understanding of the fundamental behavior of the materials we use lead

to more efficient and reliable technology. Circling back to renewable energies, research on the materials that compose solar panels is essential when looking for better solutions, not only in the realm of implementation but also in the realm of fundamental phenomena, since an in depth understanding of these materials broadens the possibilities for application. The present work aims to add to the wealth of research in this topic.

1.2 The Role of Perovskite Solar Cells

In the case of solar energy, many types of solar cells have appeared during the last decades since the first reported photovoltaic device in 1954 Chapin et al. (1954), the most recent ones being the halide perovskites solar cells Green et al. (2014). In a perovskite solar cell (PSC), a perovskite layer in the order of the hundreds of nanometers acts as the light harvester, i.e. it is a material which absorbs UV-Visible radiation generating electrons in the conduction band. This layer is in between the electron and hole transport layers (ETLs and HTLs, respectively), as shown in figure 1.2.1. Once in the conduction band, these electrons or carriers, travel through a transport pathway from the absorber layer to both electrodes. Electrons reabsorption through this pathway is a key component in power conversion efficiency (PCE), the lower the reabsorption rate, the higher the PCE. Thus, controlling perovskite formation and carefully choosing materials, carrier recombination can be suppressed in the absorber, facilitating carrier injection into the ETL, and keeping enough carrier extraction in the electrodes. The morphology of the perovskite layer has been shown to be directly related to photovoltaic properties for PSCs, so, rapid progress has been made in film processing Wang et al. (2021)Li et al. (2021) and material design Xiao et al. (2019). As a result, a broad variety of fabrication processes have been reported, but an optimized fabrication process is required in order to obtain a higher PCE. Another issue to be solved is the stability. The enviromental degradation is still one of the problems when it comes to PSCs.

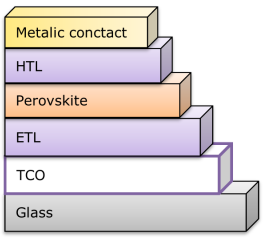

Figure 1.2.1: Simple diagram of a PSC.

Kojima *et al.* reported the first documented PSC Kojima et al. (2009), work

driven by the interest in the self-organization capabilities of perovskite in the nanoporous TiO_2 layer of dye-sensitized solar cells. Using $CH_3NH_3PbI_3$/$MAPbI_3$ and $CH_3NH_3PbBr_3$/$MAPbBr_3$ as liquid sensitizers, they achieved PCEs of 3.8% and 3.1%, respectively.
Then in 2012, Kim *et al.* obtained 9.7% PCE using $MAPbI_3$ perovskite nanoparticles and solid-state mesoscopic TiO_2 Kim et al. (2012). In 2014, the developement of two-step deposition synthesis helped PSCs jump to the 17% PCE, as reported by Im J-H. *et al.* Im et al. (2014). The same year, it was reported that a 20.1% PCE was obtained by changing perovskite composition, $(FAPbI_3)_{0.95}$/$(MAPbI_3)_{0.05}$ Cui et al. (2015). Since then, steady progress has been made, reaching 25.5% in 2019 Green et al. (2021).

1.3 An Interesting Finding

The previous section dwelled into the current state of PSC research and where the need for new development comes from, but I would like to add another source of inspiration for this work, a more personal one.
During the year 2022 I was looking into where my focus of research was going to be for my masters thesis project. Professor Noelia Benito suggested that I could look into Lead halide perovskite solar cells, specifically the perovskite layer, and so I began some preliminary tests for synthesis and imaging.
At that time the spin-caster equipment had some technical troubles that were later corrected, but that meant that some of the test samples that I synthesized were cast at low and unstable speeds, around $500RPM$ when the intended spin velocity was $2000RPM$ for example. Nevertheless, I kept with the process of analysis which included atomic force microscopy and it was then when something interesting was observed as the images from lower spin speeds where completely different from the ones cast at the intended speeds of $2000RPM$, and after discussing it further we got to the idea of studying what was going on under the the velocities commonly used for perovskite synthesis, hence a range between 600 and $1000RPM$. Some image of this preliminary tries can be seen in figure 1.3.1.
Seeing this lead to the hypothesis that we could understand the process as a deposition where film thickness would be our measure for time, therefore dynamic scaling should be applicable to our case leading to the work you are reading right now, my humble attempt at understanding new phenomena.

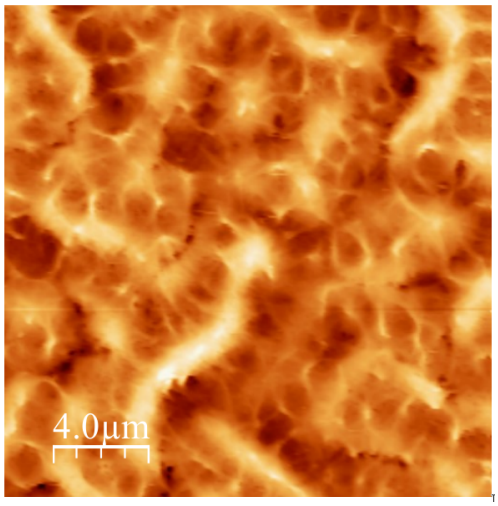

(a) 500RPM.

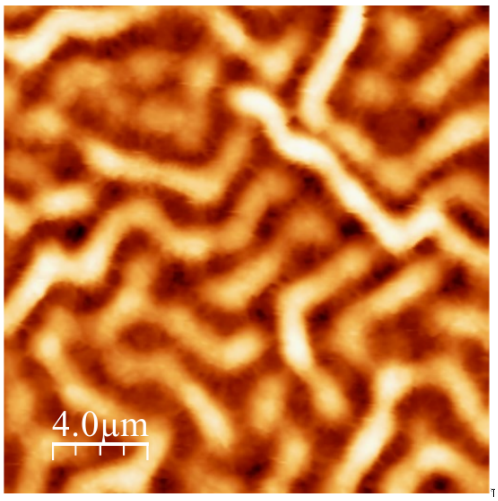

(b) 600RPM.

Figure 1.3.1: AFM images of perovskites. 1.3.1a casted at 500RPM, 1.3.1b casted at 600RPM.

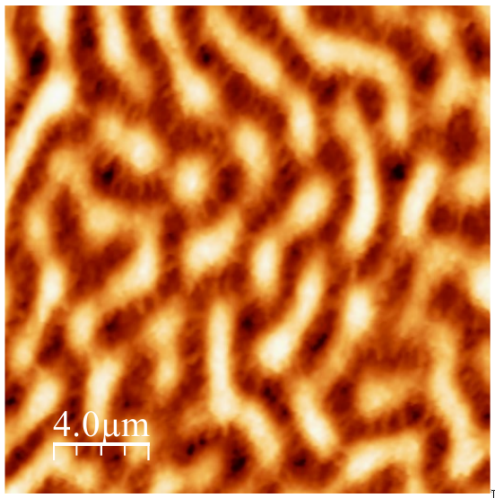

(a) 800RPM.

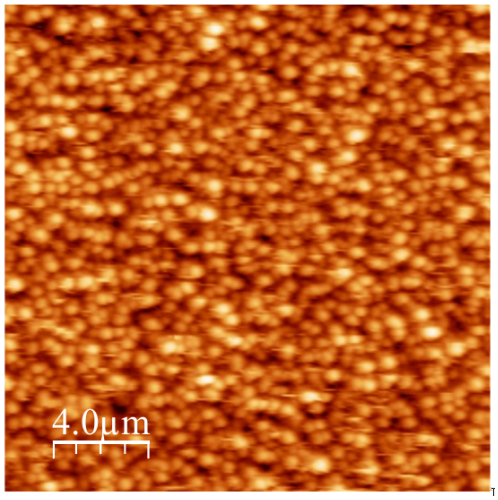

(b) 1000RPM.

Figure 1.3.2: AFM images of perovskites. 1.3.2a synthesized at 800RPM, 1.3.2b synthesized at 1000RPM.

Chapter 2

Objectives

2.1 General Objective

Use dynamic scaling to understand the growth of lead halide perovskites and their change in morphology when changing spin-casting velocity.

2.2 Specific Objectives

- To syntheisze Methylamonnioum Lead (MAI-PbI_2) perovskites at different spin-casting velocities.
- To corroborate synthesis via X-ray diffraction characterization.
- To characterize the samples by atomic force microscpy.
- To relate spin-casting velocity to thickness.
- To apply dynamic scaling theory with thicknes as measurement for time.
- To corroborate that this method is viable by comparing calculated exponents with empirical exponents.

Chapter 3

Theoretical Framework

3.1 Semiconductors

We are studying methyl ammonium lead iodide perovskite, which is a semiconductor, hence, we need to understand how a semiconductor is structured and how this structure molds electron behavior in the material. This will give us the tools needed to understand the physical properties of the material and how the different characterization methods work, notably X-Ray diffraction.

3.1.1 From lattices to crystalline structure

Let us envision how a solid is organized at an atomic level. Each atom (or group of atoms) can be thought of as a point, which are periodically arranged extending infinitely forming a **lattice**. If we were to stand on one of these points, look around, then jump to another point and repeat, we would see that the landscape looks identical from each position, that is, there is translational symmetry in the lattice. Lattices which present this kind of symmetry are known as **Bravais lattice**.

To properly define the jumps between points we first need a point of origin and as many directions as the space has dimensions. Thankfully for us we are working with just three dimensions and the origin can be any of the points in the lattice as it is symmetric under these jumps. With the starting point selected and the

three vectors needed, we can describe each point of the lattice as follows,

$$\vec{r_i} = x_i a + y_i b + z_i c \tag{3.1.1}$$

where $\vec{r_i}$ is the position is the i-th point, a, b and c are the spacial vectors and the components x_i, y_i, z_i are numbers that tell us how much we move in each of the vectors direction. Figure 3.1.1 shows the lattice with the base composed by the three vectors. They are called **primitive vectors** and allow the definition of translation, denoted by the x_i, y_i and z_i coefficients, each of them being integers, therefore generating the whole lattice.

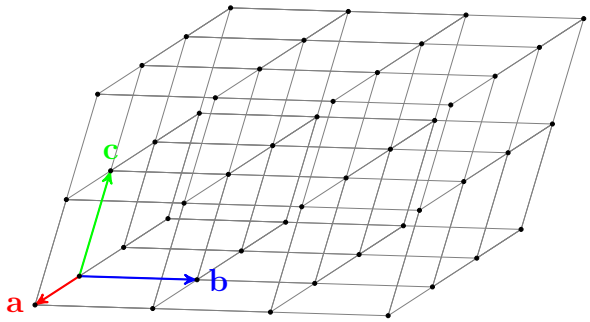

Figure 3.1.1: Bravais lattice with the basis overlayed.

As we said before, origin selection is arbitrary as many arrangements could recreate the lattice, but, when the volume of the array contains just one lattice point it becomes a **primitive cell**. This cell can be repeated without ever needing to overlap with itself in order to reproduce the whole of the material. Further more, a lattice point can be contained by positioning it at the center of the cell, as shown in figure 3.1.2a or by making each corner the center of a point. It is important to note that although we call them points, they are still considered spheres with a volume that can be divided, as shown in figure 3.1.2b.

Considering just the sphere sections inside the parallelepiped, we can see that they sum up to one sphere volume, therefore, there is one lattice point inside the cell.

Note that a primitive cell does not have any restriction to preserve the symmetry of the lattice be it rotational or otherwise, hence, a primitive cell that presents the symmetries of the lattice is a special type called the **Wigner-Seitz Cell**. We shall see that this primitive cell corresponds to the Brillouin zone defined in the

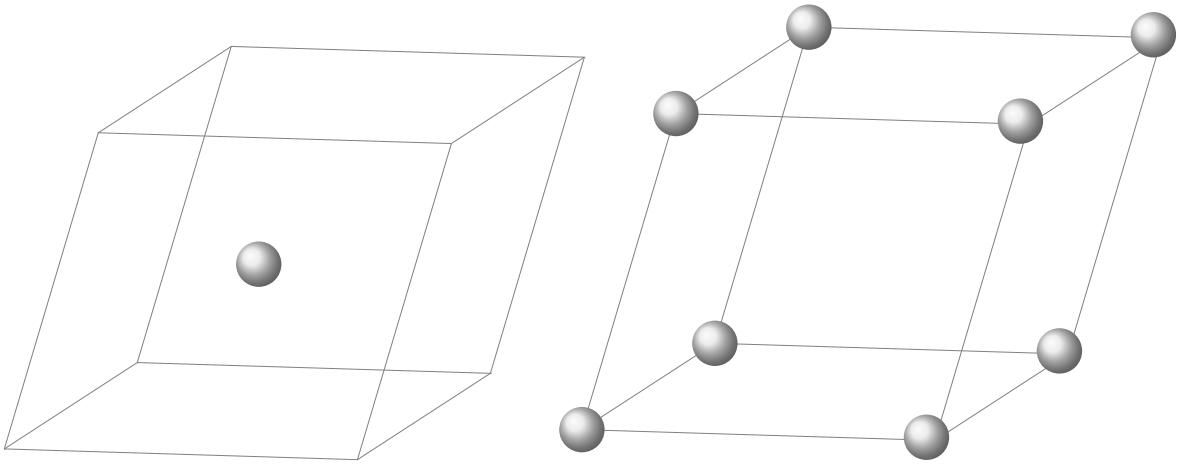

(a) Lattice point in center. **(b)** Lattice point distributed on its corners.

Figure 3.1.2: Primitive cells.

reciprocal lattice.

Continuing with the lattice, we could examine a portion or subset of the structure and describe it mathematically as we previously did with the whole of the system, yielding a new base cell or **unit cell**. A unit cell is such that, by way of translations and without overlapping, elapses a subset of the Bravais lattice and has all of its symmetries. For example, we have the body centered cell shown in figure 3.1.3, where aside from the points in its corners, it has a point in the center of the cube. In general, a unit cell has greater volume than a primitive cell, but is more useful

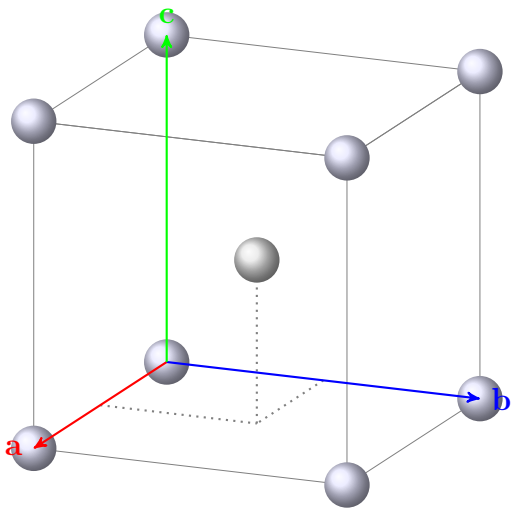

Figure 3.1.3: Body centered cell or BCC.

when it comes to analyze more complex lattices or materials with more than one

atom type.
This unit cell contains all the structures needed to replicate the lattice (atoms, ions, molecules, functional group, etc), therefore, it serves as a building block or a **basis** that encapsulates all of the properties of a given material.
By giving the lattice a structure we finally arrive at the concept of **Crystal structure**, or as Kittel succinctly puts it:

$$\text{Lattice} + \text{Basis} = \text{Crystal structure}. \tag{3.1.2}$$

3.1.2 Reciprocal lattice

Due to the periodic nature of the structure, it is of great help to use Fourier analysis, that is, obtaining the frequency representation of the original space also called **direct lattice**. First, we define $\vec{R}$ as the displacement vector that describe all points in the Bravais lattice. Using a plane wave with wave vector $\vec{k}$, the following needs to hold for $\vec{k}$ to be in the reciprocal lattice and preserve the periodicity,

$$e^{i\vec{k}\cdot(\vec{r}+\vec{R})} = e^{i\vec{k}\cdot\vec{r}} \tag{3.1.3}$$

for any $\vec{r}$ and all $\vec{R}$. This will limit the wave vectors to a set such that

$$e^{i(\vec{k}\cdot\vec{R})} = 1. \tag{3.1.4}$$

The set then defines the reciprocal lattice of the direct lattice. Of course, one could start from a reciprocal space and reconstruct the direct lattice doing the inverse process.
This mathematical treatment will be important when describing the potential for an electron in a crystal.

3.1.3 Unit cells

Until now we have consider translational symmetry to define a unit cell, but depending on the lattice we might need other symmetries such as rotation about the axis that passes through a lattice point as can be seen in the example in figure 3.1.4. The first rotation to consider is one complete rotation or 2π, meaning that the lattice will look the same with one complete rotation. Lattices can present this symmetry in fractions of a rotation to, specifically 1/2, 1/3, 1/4 and 1/6 of a

rotation. Considering the complete rotation they receive the label 1, 2, 3, 4 and 6. It is important to notice that a single array of atoms could have infinite degrees of rotational symmetry but infinite periodic lattices can't and they are restricted to the rotations mentioned before. We also have to consider that a unit cell could

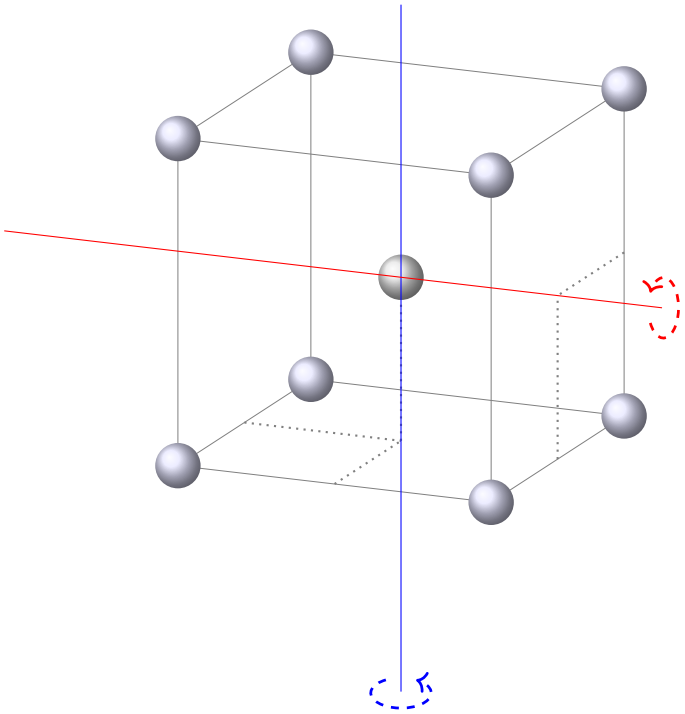

Figure 3.1.4: Two rotational axes for a body centered unit cell.

have angles different from 90 degrees and sides of different length which leads to fourteen different unit cells that can be organized in seven different systems, being the orthorombic and tetragonal the ones that interest us for the purposes of this work. They are characterized by the lengths of the unitary vectors and the angles between them (table 3.1.1 summarizes their characteristics), where the orthorombic system has different length for each side and the tetragonal system having two equal sides, all angles between them being right angles as shown in figure 3.1.5.

System	Conditions
Orthorombic	$a \neq b \neq c$ $\alpha = \beta = \gamma = \pi/2$
Tetragonal	$a = b \neq c$ $\alpha = \beta = \gamma = \pi/2$

Table 3.1.1: Characteristics of the unitary cells of interest.

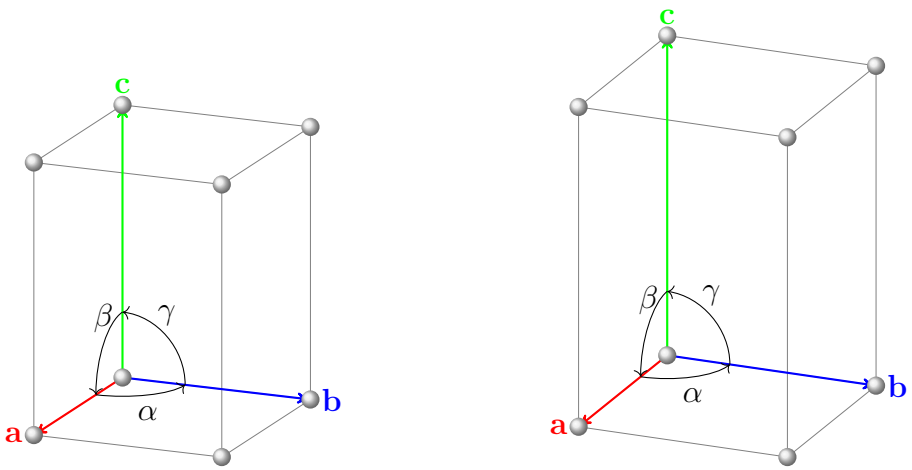

(a) Orthorombic structure. **(b)** Tetragonal structure.

Figure 3.1.5: Schematic drawing of the orthorombic and tetragonal cells.

3.1.3.1 Lattice planes

There is another important mathematical concept that greatly aids when understanding the properties of a crystal, **lattice planes**.

A plane can be defined with three non colinear lattice points such that they are contained by the plane. Because the Bravais lattice is infinite and periodic, there will be an infinite amount of parallel planes separated by a distance d, with these planes conforming a **family of planes**. For each family there is a normal vector $\hat{n}$, as shown in figure 3.1.6, such that any reciprocal vector parallel to $\hat{n}$ can be written as $\vec{K} = \frac{2\pi}{d}\hat{n}$, with the shortest being $\frac{2\pi}{d}$ in length.

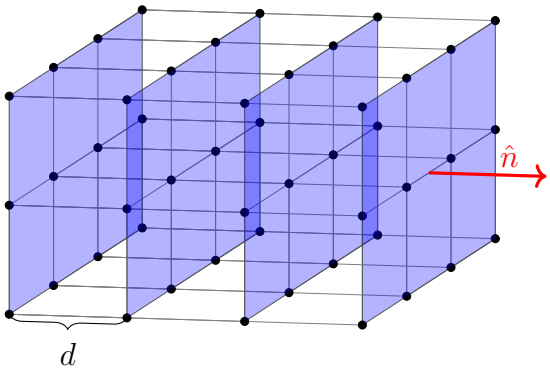

Figure 3.1.6: Family of planes in a Bravais lattice.

Considering this vector $\vec{K}$, $e^{i(\vec{K}\cdot\vec{r})}$ will be the same constant for any point in a given plane, constant value that will be the same for each plane in the family due to separation d between them. Moreover, because some planes will contain the

origin, it must be equal to 1. As for the lower limit for the vector length, if $\vec{k}$ is shorter than $\frac{2\pi}{d}$, the wavelength would be greater than d, breaking periodicity. Now, from (3.1.4), we know that this defines a reciprocal vector, therefore, $\vec{K}$ is a reciprocal vector.
From here, it is clear that the relation of planes in the direct space and reciprocal vectors is a profound one, letting us specify orientations of the lattice planes through these vectors. Further more, a reciprocal vector will encapsulate a whole family of lattice planes and by using the shortest of the reciprocal vectors one makes that choice a unique one, introducing us to the next topic.

3.1.3.2 Miller indices

We can define a set of primitive reciprocal vector **a'**, **b'**, **c'**, as we did in the direct space. Now, consider the shortest reciprocal vector perpendicular to a family of planes; this vector can be written with respect to the primitive reciprocal vectors as

$$\vec{K} = h\mathbf{a'} + k\mathbf{b'} + l\mathbf{c'}, \tag{3.1.5}$$

where every $\vec{K}$ will be normal to a plane with indices $h, k, l, \in \mathbb{Z}$. These indices are known as **Miller Indices**.
As established before, the dot product of a reciprocal vector, normal to a plane, with any of the points in the plane will be a constant, lets call it A. Now, the plane will intersect the direct lattice axes at some point, and so the question is, what relation do the Miller indices have with these intersections?

Using the direct primitive vectors, the plane will intersect the axes at some point $x_a\mathbf{a}$, $x_b\mathbf{b}$ and $x_c\mathbf{c}$, and since they belong in the plane with equation

$$\vec{K} \cdot \vec{r} = A \tag{3.1.6}$$

we have that

$$\vec{K} \cdot x_{\mathbf{a}}\mathbf{a} = A, \quad \vec{K} \cdot x_{\mathbf{b}}\mathbf{b} = A, \quad \vec{K} \cdot x_{\mathbf{c}}\mathbf{c} = A. \tag{3.1.7}$$

Since

$$\vec{K} \cdot \mathbf{a} = 2\pi h, \quad \vec{K} \cdot \mathbf{b} = 2\pi k, \quad \vec{K} \cdot \mathbf{c} = 2\pi l, \tag{3.1.8}$$

we have that the intersection occurs at the following values

$$x_{\mathbf{a}} = \frac{A}{2\pi h}, \quad x_{\mathbf{b}} = \frac{A}{2\pi k}, \quad x_{\mathbf{c}} = \frac{A}{2\pi l}, \tag{3.1.9}$$

or in other words, the intercepts are inversely proportional to the Miller indices arriving at the definition of Miller indices from crystallography:

$$h = \frac{1}{x_{\mathbf{a}}}, \quad k = \frac{1}{x_{\mathbf{b}}}, \quad l = \frac{1}{x_{\mathbf{c}}}. \tag{3.1.10}$$

The convention is that the indices of a plane are presented in the following format: (hkl). If one of the indices is negative its annotated as $\bar{i}$ (example: $(1\bar{1}1)$ is the plane with intercepts at $\mathbf{a}$, $-\mathbf{b}$ and $\mathbf{c}$). If a set of planes is equivalent to each other due to symmetries they are denoted as hkl planes.
Now, if we consider the normal vector in the direct space we get the direction of the planes and they are noted as $[n_1 n_2 n_3]$, where the points in this directions are of the type $n_1\mathbf{a} + n_2\mathbf{b} + n_3\mathbf{c}$. If a set of directions are equivalent due to symmetries they are referred as $< n_1 n_2 n_3 >$ directions.

3.1.4 X-Ray diffraction

We use x-ray diffraction to identify crystalline structures in the Results section, the basic phenomena being that of constructive interference of electromagnetic rays. In this section we will take a look at how we understand this physical effect. To understand diffraction in a crystalline structure we will use two approaches:

- Bragg's formulation
- von Laue's formulation

In Bragg's understanding of the phenomena we must envision the many planes in which a Bravais lattice can be sectioned. The fundamental assumptions are specular reflection and a monochromatic source of x-rays. The angle of the incident ray is the same as the reflected ray as shown in figure 3.1.7 and all rays have the same wavelength λ. In order for the two incident rays to present constructive interference, the optical paths must be such that, after reflection, the rays are in phase. For this to hold the wavelength of said rays has to comply with

$$n\lambda = 2d\sin(\theta) \tag{3.1.11}$$

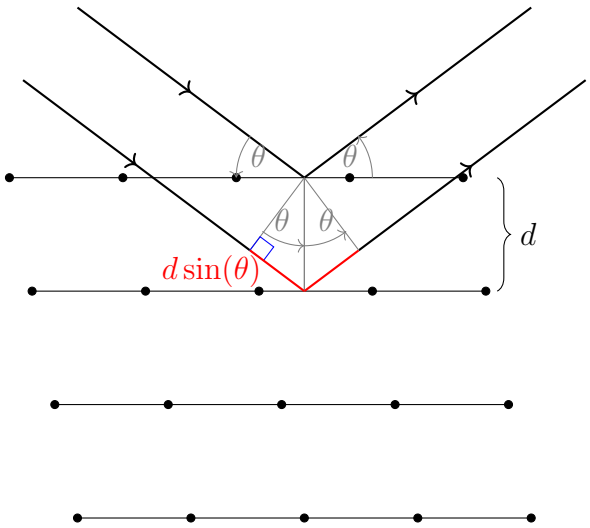

Figure 3.1.7: Bragg's diffraction.

where n is the order of the diffraction and relates to the distances between planes being considered. This is the **Bragg condition**.
In this formulation, the relation between diffraction and the planes in the direct lattice is evident. But, we can section the crystal in a myriad of ways and depending on the wavelength, different diffraction peaks will be observed. It is at this point where von Lue's approach is helpful since, instead of looking at the direct lattice, we understand diffraction using the reciprocal vectors.
Firstly, some assumptions:

- for any incident ray, each point in the lattice re-radiates radially
- the incident ray comes from far away, therefore, can be thought as a plane wave with wave vector $\vec{k} = \frac{2\pi\hat{n}}{\lambda}$, λ being the wavelength.

Envision then two points at a distance d as shown in figure 3.1.8, where $\vec{d}$ is a vector of displacement with length equal to d.

Then, the direction of the incident ray is $\hat{n}$ and with angle θ, and the scattered ray will have direction $\hat{n}'$ and angle θ', with a wave vector $\vec{k}' = \dfrac{2\pi}{\lambda}\hat{n}'$. Here, the difference in optical paths can be obtained as

$$d\cos(\theta) + d\cos(\theta') = \vec{d}\cdot(\hat{n} - \hat{n}') \tag{3.1.12}$$

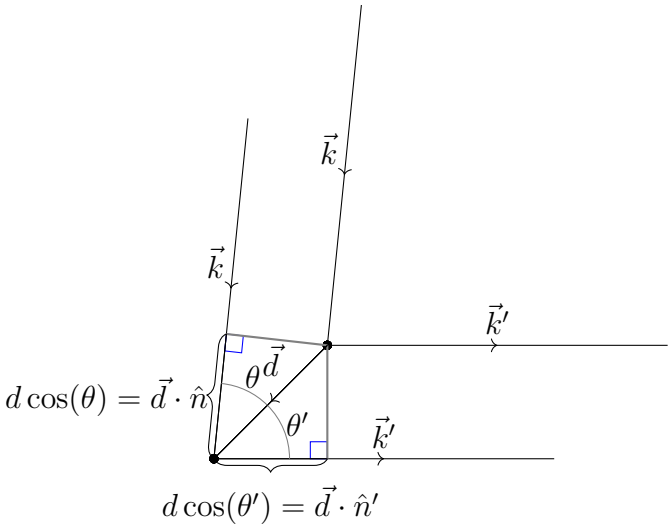

Figure 3.1.8: Difraction from two lattice points.

For it to be constructive interference, then the next needs to be true,

$$\vec{d}\cdot(\vec{k}-\vec{k}') = m\lambda, \quad \lambda \in \mathbb{Z} \tag{3.1.13}$$

$$\Rightarrow \vec{d}\cdot(\vec{k}-\vec{k}') = 2\pi m. \tag{3.1.14}$$

This is for two points, but taking in consideration the first assumption, we need to consider every point in the lattice so that, for a diffraction peak to show, the scattered rays from all points need to constructively interfere. Now, in (3.1.3) we defined that each point in the lattice can be described by the displacement vector $\vec{R}$, therefore we can say that

$$\vec{R}\cdot(\vec{k}-\vec{k}') = 2\pi m \tag{3.1.15}$$

meaning that $\vec{k}-\vec{k}'$ is a reciprocal vector since $e^{i\vec{R}\cdot(\vec{k}-\vec{k}')} = 1$, as well as $\vec{k}'-\vec{k}$. Then, if we make the condition that both magnitudes of $\vec{k}$ and $\vec{k}'$ are the same value k we have that

$$k\cdot\vec{K} = \frac{1}{2}K \tag{3.1.16}$$

where $\vec{K} = \vec{k}-\vec{k}'$. This is known as the **Laue condition**.
This is better visualized in figure 3.1.9 where O is the origin of the reciprocal or k-space and K is the tip of the vector $\vec{K}$. Thus, for an incident ray to comply with this condition, its tip must lie in the plane that bisects the vector $\vec{K}$. This planes are known as **Bragg planes**.

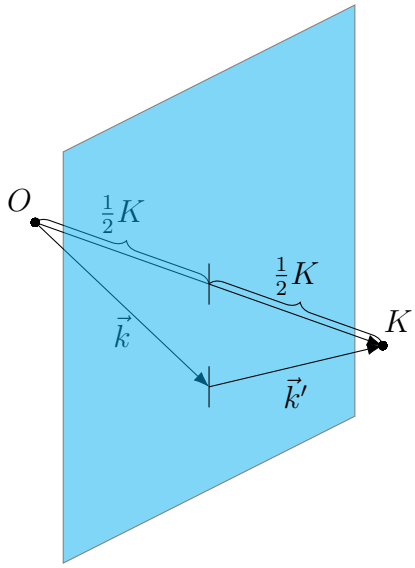

Figure 3.1.9: Depiction in the $k-$space of the Laue condition.

Because $\vec{K}$ is a reciprocal vector we can assure that it is a integer multiple of the shortest parallel reciprocal vector, thus its magnitude can be written as

$$K = \frac{2\pi}{d}n, \quad n \in \mathbb{Z}, \tag{3.1.17}$$

and, because from (3.1.12) we know that $K = 2k\sin(\theta)$, we get that

$$k\sin(\theta) = \frac{\pi}{d}n. \tag{3.1.18}$$

Further more, as $k = \dfrac{2\pi}{\lambda}$, we have proven that this wavelength satisfies Bragg condition, thus relating the order of the Bragg diffraction n with the length of the vector $\vec{K}$ that corresponds to the Laue diffraction peak.
This framework is ideal to understand the characterization method used in this work, which is X-ray diffraction analysis using a monochromatic source and varying incident angle.
First, let me introduce the Ewald sphere. In the k-space, consider a sphere with radious equal to the length of a vector $\vec{k}$ that starts at a reciprocal point O and centered on its tip, as shown in figure 3.1.10

The points that fulfill Laue condition, therefore, constructively interfere with the ray $\vec{k}$ are the ones on the surface of the sphere which is a Bragg reflection on the direct space. And, as figure 3.1.10 shows, for any reciprocal vector $\vec{k}$, most

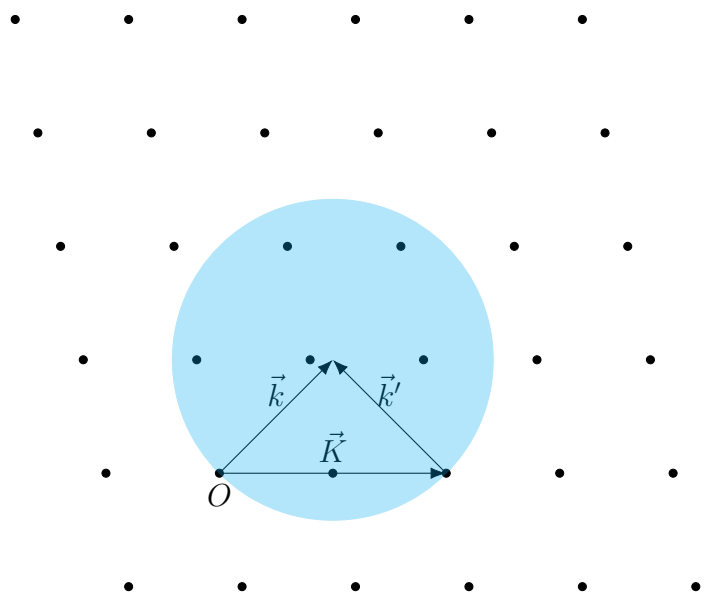

Figure 3.1.10: Ewald sphere in the $k-$space.

points will not be in the surface of said sphere, that is no diffraction peak will be generated. We can think of this sphere as describing the family of planes perpendicular to $\vec{k}$.

With this we can think of a few ways for us to find diffraction peaks, either by changing the length of $\vec{k}$ (changing wavelength), or by moving the sphere, that is, changing the angle of incidence of $\vec{k}$ or, equivalently, rotating the direct lattice and thus the reciprocal lattice. In the case of this work we are changing the incident angle around the crystal using a set wavelength.

3.1.4.1 Structure factor

Connecting this to the unit cells, is clear that each structure will have a distinct set of diffraction peaks that depends on atom or molecule positioning. The challenge is how to determine the structure from a diffraction spectrum.

First, we will deal with the case of a mono-atomic crystal. We define the positions of all n atoms in a unit cell as $\vec{d}_1, ..., \vec{d}_n$. Then, all scattered rays will depend on these positions and, as we established in the previous section, diffraction peaks are associated with a displacement reciprocal vector $\vec{K}$. Interference depends on the phase between two scattered rays, given by $\vec{K} \cdot (\vec{d}_i - \vec{d}_j)$, thus, comparing to the scattering generated by $\vec{d}_i$, the differences in amplitudes from each scattered ray has a factor of $e^{i\vec{K}\cdot(\vec{d}_i - \vec{d}_j)}$. Then, the resulting ray scattered by the whole cell

will have an amplitude

$$S_{\vec{K}} = \sum_{j=1}^{n} e^{i\vec{K}\cdot\vec{d}_j} \tag{3.1.19}$$

where $S_{\vec{K}}$ receives the name of **geometrical structure factor**, which tells us how much the intensity of the Bragg peak associated to $\vec{K}$ is diminished by interference with the basis cell and, although other factors have a role when it comes to peak intensity, the structure factor is better used to identify destructive interference. As we said at the beginning of the section, this is for the mono-atomic case, therefore, a little tweak to (3.1.19) needs to take place for it to consider the specific ion occupying any position, living us with the following

$$S_{\vec{K}} = \sum_{j=1}^{n} f_j(\vec{K}) e^{i\vec{K}\cdot\vec{d}_j}, \tag{3.1.20}$$

where f_j is called the **atomic form factor** and depends on the specific properties of the ion at the j-*th* position.

3.1.5 Band theory

What does an electron in a crystal see?
Due to the periodicity of the crystal structure one could imagine that, neglecting electron-electron interaction, a periodic potential generated by the many atom nuclei would be the answer. This also points to the wave function of the electron to be periodic, so, lets do some calculations!

3.1.5.1 Bloch's theorem

First, wee need to establish a few things:

1. The crystal does not change in time (time independence)
2. The potential has translational symmetry under integer multiples of the unitary vectors ($U(\vec{r}) = U(\vec{r} + \vec{R})$, $\vec{R}$).

With this we can define that the Shcröedinger equation for the electron is

$$\varepsilon\psi(\vec{r}) = -\frac{\hbar^2}{2m}\nabla^2\psi(\vec{r}) + U(\vec{r})\psi(\vec{r}) \tag{3.1.21}$$

where E is the energy of the electron and U is the periodic potential.
Because the potential is periodic so it is the Hamiltonian H meaning that

$$H(\vec{r}) = H(\vec{r} + \vec{R}). \tag{3.1.22}$$

So, under a translation $T_{\vec{R}}$ we get that

$$T_{\vec{R}} H(\vec{r})\psi(\vec{r}) = H(\vec{r} + \vec{R})\psi(\vec{r} + \vec{R}) = H(\vec{r})\psi(\vec{r} + \vec{R}) = H(\vec{r})T_{\vec{R}}\psi(\vec{r}), \tag{3.1.23}$$

therefore, $T_{\vec{R}}$ and H commute.
The eigenstates of the translation operator are then

$$T_{\vec{R}}\psi = c(\vec{R})\psi. \tag{3.1.24}$$

Now, for two different translations we get

$$T_{\vec{R}} T_{\vec{R}'}\psi(\vec{r}) = \psi(\vec{r} + \vec{R} + \vec{R}')\psi(\vec{r} + \vec{R}' + \vec{R}) = T_{\vec{R}'} T_{\vec{R}}\psi(\vec{r}) \tag{3.1.25}$$

thus,

$$T_{\vec{R}} T_{\vec{R}'} = T_{\vec{R}'} T_{\vec{R}} = T_{\vec{R}+\vec{R}'}. \tag{3.1.26}$$

The eigenstates of a composed translation are then

$$T_{\vec{R}+\vec{R}'}\psi = c(\vec{R} + \vec{R}')\psi \tag{3.1.27}$$

but considering (3.1.25) we get that

$$c(\vec{R} + \vec{R}') = c(\vec{R})c(\vec{R}') \tag{3.1.28}$$

We could consider translations that occur in one of the directions of the primitive basis $\mathbf{a}$, $\mathbf{b}$ or $\mathbf{c}$. The eigen values then would be

$$c(\mathbf{a}) = e^{i2\pi x_{\mathbf{a}}}, \quad c(\mathbf{b}) = e^{i2\pi x_{\mathbf{b}}}, \quad c(\mathbf{c}) = e^{i2\pi x_{\mathbf{c}}}. \tag{3.1.29}$$

But a translation vector $\vec{R}$ written in the primitive basis is

$$\vec{R} = n_{\mathbf{a}}\mathbf{a} + n_{\mathbf{b}}\mathbf{b} + n_{\mathbf{c}}\mathbf{c}, \tag{3.1.30}$$

therefore, using (3.1.28) the eigen value for $\vec{R}$ is

$$c(\vec{R}) = c(n_{\mathbf{a}}\mathbf{a} + n_{\mathbf{b}}\mathbf{b} + n_{\mathbf{c}}\mathbf{c}) \tag{3.1.31}$$
$$= c(\mathbf{a})^{n_{\mathbf{a}}} c(\mathbf{b})^{n_{\mathbf{b}}} c(\mathbf{c})^{n_{\mathbf{c}}} \tag{3.1.32}$$
$$= e^{i8\pi^3(n_{\mathbf{a}}x_{\mathbf{a}} + n_{\mathbf{b}}x_{\mathbf{b}} + n_{\mathbf{c}}x_{\mathbf{c}})} \tag{3.1.33}$$
$$= e^{i\vec{k}\cdot\vec{R}}, \tag{3.1.34}$$

where $\vec{k} = x_{\mathbf{a}}\mathbf{a'} + x_{\mathbf{b}}\mathbf{b'} + x_{\mathbf{c}}\mathbf{c'}$ and we know from the Fourier transform that $\mathbf{a}\cdot\mathbf{a'} = 2\pi$, $\mathbf{b}\cdot\mathbf{b'} = 2\pi$, $\mathbf{c}\cdot\mathbf{c'} = 2\pi$.
So, we can choose ψ eigenstate of H so that for every vector $\vec{R}$

$$T_{\vec{R}}\psi = c(\vec{R})\psi = e^{i\vec{k}\cdot\vec{R}}\psi(\vec{r}), \tag{3.1.35}$$

meaning that, for a periodic potential, eigenstates of the Hamiltonian translated by a vector $\vec{R}$ only differ by a phase. This is Bloch's theorem.

3.1.6 Born - von Karman condition

By using the volume of the primitive cell we can understand the periodicity condition as

$$\psi(\vec{r} + N_i\mathbf{a}_i) = \psi(\vec{r}), \quad i = 1, 2, 3 \tag{3.1.36}$$

where $\mathbf{a}_i$ are the primitive vectors and N_i are integers, with $N = N_1N_2N_3$ the total number of primitive cells in the crystal.
Applying (3.1.35) to (3.1.36) we get

$$\psi_{n\vec{k}}(\vec{r} + N_i\mathbf{a}_i) = e^{iN_i\vec{k}\cdot\mathbf{a}_i} \tag{3.1.37}$$

requiring

$$e^{iN_i\vec{k}\cdot\mathbf{a}_i} = 1, \tag{3.1.38}$$

which when using (3.1.34) transforms into

$$e^{i2\pi N_i x_i} = 1 \tag{3.1.39}$$
$$\Rightarrow x_i = \frac{m_i}{N_i}, \quad m_i \in \mathbb{Z}. \tag{3.1.40}$$

Hence, $\vec{k}$ can only be of the form

$$\vec{k} = \sum_{i=1}^{3} \frac{m_i}{N_i} \mathbf{b}_i \tag{3.1.41}$$

with $\mathbf{b}_i$ being the reciprocal primitive vectors.
Every vector $\vec{k}$ will define a volume of the $k-$space

$$\Delta\vec{k} = \frac{\mathbf{b}_1}{N_1} \cdot \left(\frac{\mathbf{b}_2}{N_2} \times \frac{\mathbf{b}_3}{N_3} \right) \tag{3.1.42}$$

$$= \frac{1}{N} \mathbf{b}_1 \cdot (\mathbf{b}_2 \times \mathbf{b}_3) \tag{3.1.43}$$

$$= \frac{1}{N} V'_{\mathbf{prim}} \tag{3.1.44}$$

where $V'_{\mathbf{prim}}$ is the volume of the reciprocal primitive cell.
This means that the number of allowed $\vec{k}$ in a reciprocal primitive cell is equal to the number of reciprocal primitive cells in the crystal.
Because direct and reciprocal primitive cell volumes are related as

$$V_{\text{prim}} = \frac{(2\pi)^3}{V'_{\text{prim}}} \tag{3.1.45}$$

with V_{prim} the volume of the direct primitive cell, we obtain the volume section of the $k-$space as

$$\Delta\vec{k} = \frac{(2\pi)^3}{V_{prim}}. \tag{3.1.46}$$

3.1.7 Bloch functions

As noted in the previous section, if a vector fulfills the periodic condition (3.1.37) it will be a vector of the form (3.1.41), so if a wave vector does satisfy the boundary condition it can be written as

$$\psi(\vec{r}) = \sum_{\vec{q}} c_{\vec{q}} e^{i\vec{q}\cdot\vec{r}}. \tag{3.1.47}$$

As established before the potential is periodic, therefore it admits an expansion in the reciprocal lattice as

$$U(\vec{r}) = \sum_{\vec{K}} U_{\vec{K}} e^{i} \vec{K} \cdot \vec{r}, \tag{3.1.48}$$

where the coefficients $U_{\vec{K}}$ are the Fourier transform of $U(\vec{r})$.
Applying (3.1.47) and (3.1.48) to the Schrodinger equation we obtain

$$\varepsilon \sum_{\vec{q}} c_{\vec{q}} e^{i\vec{q}\cdot\vec{r}} = \frac{\hbar^2}{2m} \sum_{\vec{q}} q^2 e^{i\vec{q}\cdot\vec{r}} + \sum_{\vec{K}} \sum_{\vec{q}} U_{\vec{K}} c_{\vec{q}} e^{i(\vec{K}+\vec{q})\cdot\vec{r}}. \tag{3.1.49}$$

Making $\vec{q'} = \vec{K} + \vec{q}$ we can write the potential term as

$$\sum_{\vec{K}} \sum_{\vec{q}} U_{\vec{K}} c_{\vec{q}} e^{i(\vec{K}+\vec{q})\cdot\vec{r}} = \sum_{\vec{K}} \sum_{\vec{q'}} U_{\vec{K}} c_{\vec{q'}-\vec{K}} e^{i\vec{q'}\cdot\vec{r}}. \tag{3.1.50}$$

Because $\vec{q'}$ is also a reciprocal vector we can change indices as $\vec{q'} \to \vec{q}$, $\vec{K} \to \vec{K'}$, so that the Schrodinger equation is

$$\varepsilon \sum_{\vec{q}} c_{\vec{q}} e^{i\vec{q}\cdot\vec{r}} = -\frac{\hbar^2}{2m} \sum_{\vec{q}} q^2 e^{i\vec{q}\cdot\vec{r}} + \sum_{\vec{K'}} \sum_{\vec{q}} U_{\vec{K'}} c_{\vec{q}-\vec{K}} e^{i\vec{q}\cdot\vec{r}}. \tag{3.1.51}$$

By grouping terms on $e^{i\vec{q}\cdot\vec{r}}$ we get

$$\sum_{\vec{q}} c_{\vec{q}} e^{i\vec{q}\cdot\vec{r}} \left[\left(\frac{\hbar^2}{2m} q^2 - \varepsilon \right) c_{\vec{q}} + \sum_{\vec{K'}} U_{\vec{K'}} c_{\vec{q}-\vec{K'}} \right] = 0. \tag{3.1.52}$$

The set of $\vec{q}$ is an orthogonal set, therefore

$$\left(\frac{\hbar^2}{2m} q^2 - \varepsilon \right) c_{\vec{q}} + \sum_{\vec{K'}} U_{\vec{K'}} c_{\vec{q}-\vec{K'}} = 0. \tag{3.1.53}$$

Now, if we write $\vec{q}$ as $\vec{k} - \vec{K}$, where $\vec{K}$ is chosen so that $\vec{k}$ lies in the first Brillouin zone, we get the following condition

$$\left(\frac{\hbar^2}{2m} (\vec{k} - \vec{K})^2 - \varepsilon \right) c_{\vec{k}-\vec{K}} + \sum_{\vec{K'}} U_{\vec{K'}} c_{\vec{k}-\vec{K}-\vec{K'}} = 0. \tag{3.1.54}$$

With a change of variable for the potential $\vec{K'} \to \vec{K'} - \vec{K}$ we obtain

$$\left(\frac{\hbar^2}{2m} (\vec{k} - \vec{K})^2 - \varepsilon \right) c_{\vec{k}-\vec{K}} + \sum_{\vec{K'}} U_{\vec{K'}-\vec{K}} c_{\vec{k}-\vec{K'}} = 0. \tag{3.1.55}$$

For $\vec{k}$ in the first Brillouin zone, all coefficients $c_{\vec{k}-\vec{K}'}$ are for vectors that differ from $\vec{k}$ a reciprocal lattice vector, therefore, each allowed k defines a plane wave solution containing just the one vector $\vec{k}$ and vectors that of the type $\vec{k}-\vec{K}'$, there being N allowed vectors $\vec{k}$ as stated in (3.1.44), hence restricting the values for $\vec{q}$ in (3.1.47).
With this, we can write (3.1.47) as

$$\psi_{\vec{k}} = \sum_{\vec{K}} c_{\vec{k}-\vec{K}} e^{i(k-\vec{K})\cdot\vec{r}} \tag{3.1.56}$$

$$= u(\vec{r}) e^{i\vec{k}\cdot\vec{r}}, \tag{3.1.57}$$

where we define the periodic function

$$u(\vec{r}) = \sum_{\vec{K}} c_{\vec{k}-\vec{K}} e^{-i\vec{K}\cdot\vec{r}}. \tag{3.1.58}$$

Note that (3.1.57) is of the form (3.1.35), so we have re-stated Bloch's theorem but from looking at the Born - von Karman condition and how it restricts the allowed reciprocal vectors.

3.1.8 Energy bands: Kronig-Penney model

To understand how the potential will look like lets consider the one dimensional case where the Schrodinger equation for the electron is

$$\varepsilon\psi(x) = -\frac{\hbar^2}{2m}\frac{\mathrm{d}^2\psi}{\mathrm{d}x^2} + U(x). \tag{3.1.59}$$

The potential U will be a square-well repeating pattern as figure 3.1.11, where the value is non 0 for the spots with ions.

In the region $0 < x_1 < a$ where the potential is 0, the free electron wave function will be a plane wave

$$\psi(x_1) = Ae^{iKx_1} + Be^{-iKx_1} \tag{3.1.60}$$

and the energy reducing to the kinetic energy

$$\varepsilon = \frac{\hbar^2}{2m}K^2, \tag{3.1.61}$$

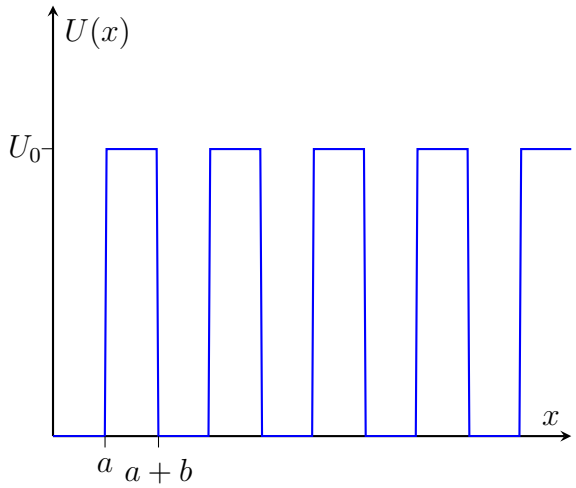

Figure 3.1.11: Periodic square-well.

while in the region $-b < x_2 < 0$ where the potential has value U_0 the wave function and energy will be

$$\psi(x_2) = Ce^{Qx_2} + De^{-Qx_2} \tag{3.1.62}$$

$$\varepsilon = U_0 - \frac{\hbar^2}{2m}Q^2. \tag{3.1.63}$$

Because there is periodicity in the potential we know that it can be written as (3.1.57), therefore the solution in both region are related by

$$\psi(x_1) = \psi(x_2)e^{ik(a+b)}. \tag{3.1.64}$$

Further more, the function and its derivative are continuous so at $x = 0$ we obtain the system of equations

$$A + B = C + D \tag{3.1.65}$$

$$iK(A - B) = Q(C - D). \tag{3.1.66}$$

On the other hand, at $x = a$ and thanks to (3.1.64) we can get the following equation system

$$Ae^{iKa} + B^{-iKa} = (Ce^{-Qb} + De^{Qb})e^{ik(a+b)} \tag{3.1.67}$$

$$iK(Ae^{iKa} - B^{-iKa}) = Q(Ce^{-Qb} + De^{Qb})e^{ik(a+b)}. \tag{3.1.68}$$

For the whole system to have a solution if the determinant of coefficients A, B, C and D must vanish, which, after some calculations (Kittel and McEuen (2018)), occurs when

$$\frac{Q^2 - K^2}{2QK} \sinh Qb \sin Ka + \cosh Qb \cos Ka = \cos k(a + b). \tag{3.1.69}$$

Now, if we set $U_0 \to \infty$ and $b \to 0$ we can express the potential as a periodic Dirac's delta, reducing the solution to

$$\frac{P}{Ka} \sin Ka + \cos Ka = \cos ka, \quad P = \frac{Q^2 ba}{2}, \tag{3.1.70}$$

The right side of the equation oscilates between ± 1, meaning that the system has non trivial solutions in the regions where the left side lies between ± 1, while outside this range there are no solutions with the form (3.1.57). Solving for K and multiplying by a in (3.1.61) we can see the relation between Ka and ε,

$$Ka = \sqrt{\frac{2m\varepsilon}{\hbar^2}} a, \tag{3.1.71}$$

therefore, we also have restricitons for energy values.

In other terms, because we don't have an analytical solution for ε we have to reconstruct it based on the restriction for Ka by taking the intervals of Ka where the left hand side of (3.1.70) is in the region ± 1. We can build the energy spectrum by taking the allowed portions of the function and mapping them to the periodicity in k given by a.

A plot of the left side is shown in 3.1.12 where the gaps between allowed values are the **energy band gaps** of the energy spectrum, while in figure 3.1.13 the energy spectrum is shown.

If we take a look at the effects of P it can be noted that by making $P \to 0$ any Ka will sufice, meaning that we recover the free electron case, while if we do $P \to \infty$ the solution reduces to just one case where $Ka = 0$, which is the case of an electron in a infinite square well with quantize energy spectrum $\varepsilon = \dfrac{n^2\hbar^2}{2ma^2}$.

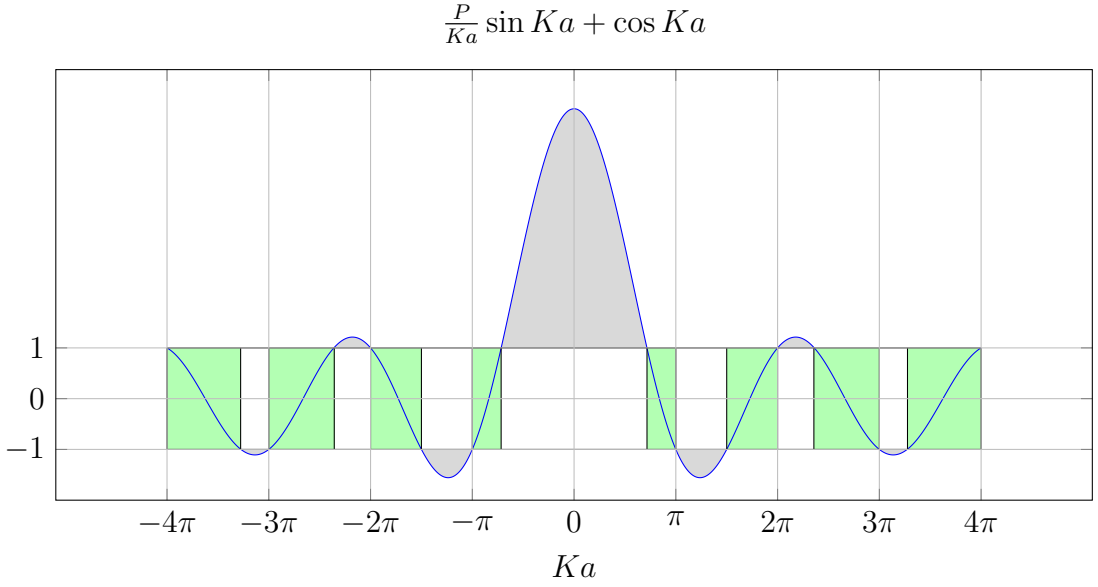

Figure 3.1.12: Plot of $\frac{P}{Ka}\sin Ka + \cos Ka$ for $P = \dfrac{3\pi}{2}$. The gray areas show the region with no non-trivial solution while the green area denotes the region where ψ is of the form (3.1.57).

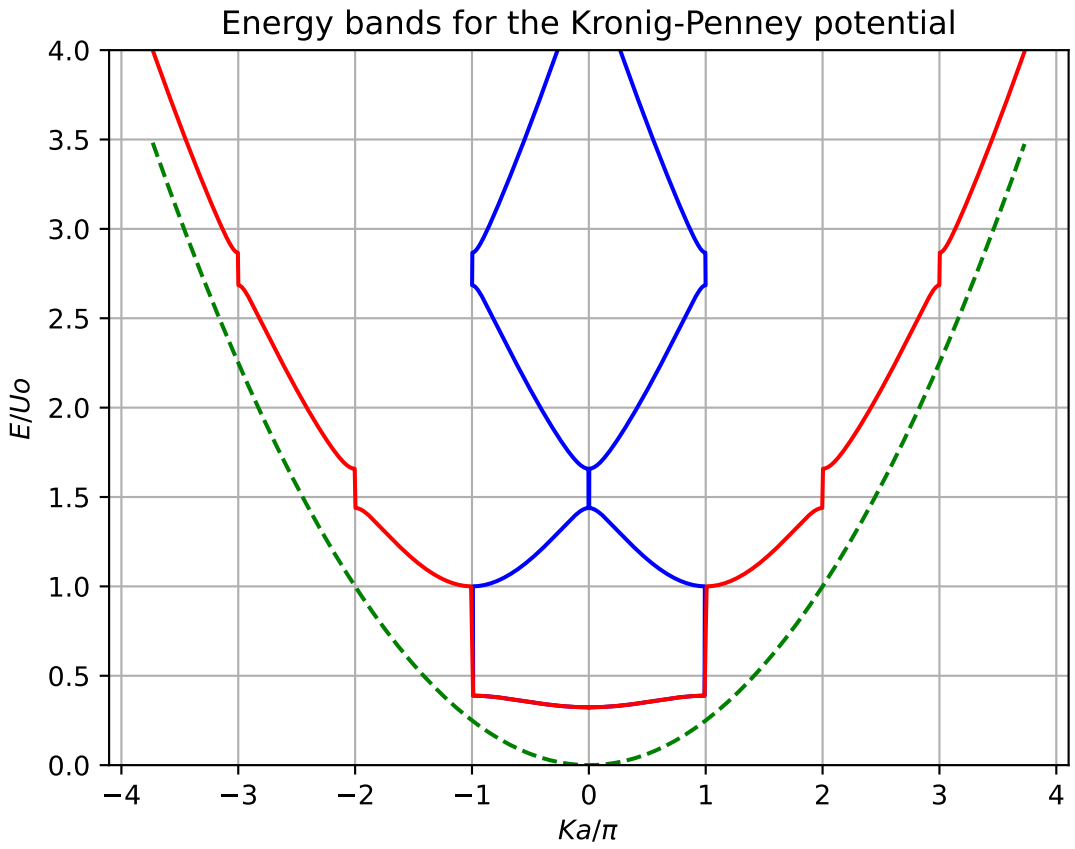

Figure 3.1.13: Band structure of the Kronig-Penney potential. The dashed green line corresponds to the parabolic potential for a single source, the red line is the potential for the infite array with the energy gaps as the vertical lines. The blue line represents the same as the red line but mapped into the first region (-1 to 1).

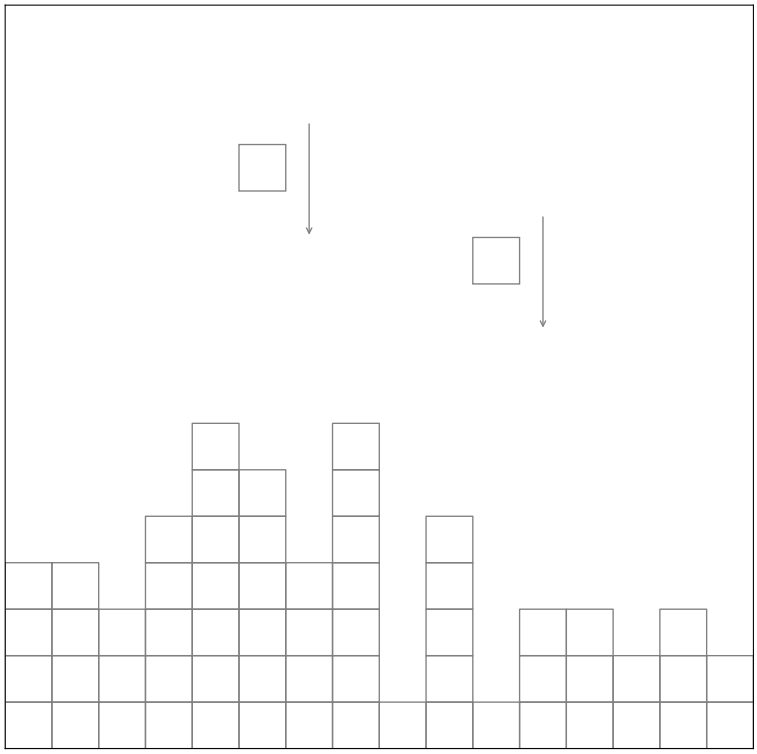

Figure 3.2.1: Random deposition diagram particle by particle.

3.2 Dynamic scaling theory

What are we studying in material surfaces? When abstracted to its basic components, we are trying to understand how the height profile of this surface changes. In order to do this, lets set two main assumptions:

1. Tthe growth process can be understood as randomly dropping units of material over a substrate, diagram of the process seen in figure 3.2.1.

2. This distribution of material generates different heights on each point of the substrate. We call this height profile the **height function** h, as shown in figure 3.2.2.

The height function will be dependent on spatial coordinates (where we stand on the substrate) and time, due to the fact that the depositions are random, thus, h's graph might change over time. Therefore, $h = h(\vec{x}, t)$, where in principle $\vec{x}$ can be $d-$dimensional. At first glance, one might think that using a inherently random model is counter productive, but the last piece of our system is the fact that,

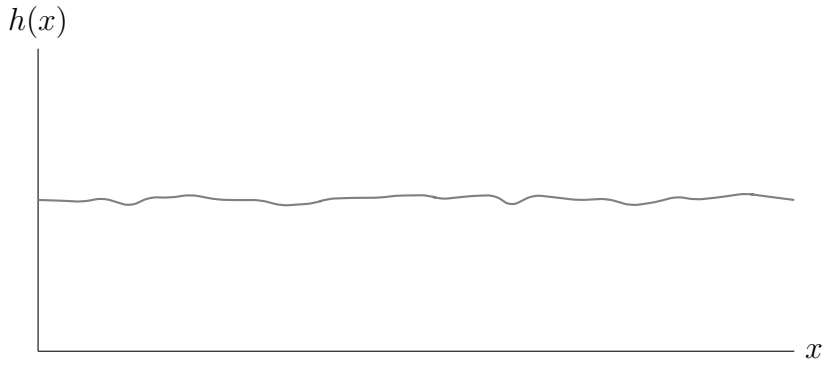

Figure 3.2.2: A random profile described by the funtion h.

at sufficiently long times, the random part of the model will obey a symmetric distribution, with mean 0, variance or diffusion D and disregard higher order momentum.
With the stage set up, we can continue our journey.

3.2.1 Height and roughness

As was established before, our object of study will be the height function h, whose evolution will depend on random phenomena. As such, this problem requires the statistical analysis of the height function $\bar{h}$ and the standard deviation w.
For a one dimensional substrate of size L we will have that,

$$\bar{h}(t) = \frac{1}{L}\sum_{i=1}^{L} h(\vec{x}_i, t) \tag{3.2.1}$$

$$w(L,t) \equiv \sqrt{\frac{1}{L}\sum_{i=1}^{L}[h(\vec{x}_i, t) - \bar{h}(t)]^2}. \tag{3.2.2}$$

where $\vec{x}_i$ is the point in space associated with the ith section of the substrate.
The standard deviation is a quantitative assessment of how much the height function deviates from its mean, in other words, it is a measurement of the surface **roughness**. With time, the mean will grow linearly as the process is about stacking material units on top of each other ($\bar{h} \sim t$). On the other hand, it is not clear that the standard deviation has a linear dependence in time, as it is determined by the randomness of the process, but it will saturate for a value (w_{sat}) at a given time (t_{sat}). During the time period previous to saturation, we will have

that,

$$w(L,t) \sim t^{\beta} \tag{3.2.3}$$

giving β the name of **growth exponent**. This time elapsing from start to saturation is the dynamic part of the process, and from that point onward, roughness will not be significantly modified by adding more material to the system.

As for the size dependency of $h(L,t)$ and its effects on the saturation width, we have that as it was the case with time dependency, it obeys a power law (but this time of size L), and it will give us information about the horizontal correlation in the sample.

$$w_{\text{sat}}(L) \sim L^{\alpha} \tag{3.2.4}$$

where α is called **roughness exponent**.

The size of the sample not only determines the saturation value but also the time at which it is achieved, obeying the same power law but with different exponent, and because delimits the dynamic part of the process it is called the **dynamic exponent**

$$t_{\text{sat}} \sim L^{z}, . \tag{3.2.5}$$

The inter-dependency of these exponents is noticeable if we approach the saturation point from the dynamic region and the saturated region. At the saturation time $w(t_{\text{sat}}) = w_{\text{sat}} \sim t_{\text{sat}}^{\beta}$, but (3.2.4) and (3.2.5) also hold, therefore α, β and z are related as follows

$$t_{\text{sat}}^{\beta} \sim L^{\alpha} \tag{3.2.6}$$

$$\Rightarrow z = \frac{\alpha}{\beta} \tag{3.2.7}$$

A sort of normalization can be done by dividing w by w_{sat}, and by replacing dependencies on L we get to the Family-Vicsek scaling relation

$$w(L,t) \sim L^{\alpha} f\left(\frac{t}{L^{z}}\right) \tag{3.2.8}$$

3.2.2 An expression for the height function

Now that we want to understand the height function in time, that is, we want a solution for $\partial_t h(\vec{x}, t)$.
In general, it could be any function $G(h, \vec{x}, t)$, but we need to add random noise to account for the randomness of the process,

$$\partial_t h(\vec{x}, t) = G(h, \vec{x}, t) + \eta(\vec{x}, t) \tag{3.2.9}$$

where η is the noise function. The properties of the mean and second moment for the noise function are as follows

$$\langle \eta \rangle = 0 \tag{3.2.10}$$

$$\langle \eta(\vec{x}, t)\eta(\vec{x}', t') \rangle = 2D\delta(\vec{x} - \vec{x}')\delta(t - t') \tag{3.2.11}$$

where D is the diffusion value of the distribution.
First we need to establish the properties of the function G we are looking for, i.e. define its symmetries. For this we will consider five symmetries:

- Invariant under time translation

$$\partial_t G(h, \vec{x}, t) = \partial_{\delta_t} G(h, \vec{x}, t + \delta_t) \tag{3.2.12}$$

- Invariant under space translation parallel to growth direction

$$\nabla G(h, \vec{x}, t) = \nabla G(h + \delta_h, \vec{x}, t) \tag{3.2.13}$$

- Invariant under space translation perpendicular to growth direction

$$\nabla G(h, \vec{x}, t) = \nabla G(h, \vec{x} + \delta_x, t) \tag{3.2.14}$$

- Invariant under rotation or inversion with the growth direction as rotation axis

$$\frac{\partial G(h, \vec{x}, t)}{\partial x^i} = \frac{\partial G(h, \vec{x}, t)}{\partial(-x^i)} \tag{3.2.15}$$

- Symmetry to fluctuations with respect to the mean height and its direction

$$\partial_t G(h, \vec{x}, t) = \partial_t G(-h, \vec{x}, t) \tag{3.2.16}$$

From these symmetry principles we obtain that the only expressions that comply with all of them are of the following type

$$G(h) = (\nabla^2 h) + \cdots + (\nabla^{2n} h) + (\nabla^2 h)(\nabla h)^2 + \cdots + (\nabla^{2m} h)(\nabla h)^{2l} \tag{3.2.17}$$

where $n, m, l \in \mathbb{N}^+$.

The equation we are dealing is then

$$\partial_t h(\vec{x}, t) = (\nabla^2 h) + \cdots + (\nabla^{2n} h) + (\nabla^2 h)(\nabla h)^2 + \cdots + (\nabla^{2m} h)(\nabla h)^{2l} + \eta(\vec{x}, t) \tag{3.2.18}$$

If we apply the Fourier transform to (3.2.18) we obtain

$$-i\omega h(\vec{k}, \omega) = -k^2 h(\vec{k}, \omega) + \mathcal{O}(k^4) h(\vec{k}, \omega) + \eta(\vec{k}, \omega) \tag{3.2.19}$$

with k being the modulus of the wave vector. Because we are interested in long time and long distance limits ($t \to \infty$, $x \to \infty$), that is $\omega \to 0$ and $k \to 0$, we can see that the terms of order k^4 and greater will go to 0 at a greater rate than the term of order k^2 and ω. For this reason, the only term that will be sufficiently important in the evolution is $\nabla^2 h$.
Thus, the equation to be solved is

$$\partial_t h(\vec{x}, t) = \nu \nabla^2 h + \eta(\vec{x}, t) \tag{3.2.20}$$

where ν is a modulation of the smoothing effect of the Laplacian term. Equation (3.2.20)is the Edward-Wilkinson equation.

3.2.3 Re-scaling

Now that we have determined the equation that models the system, we need to see how it is affected by re-scaling, that is, to find an expression for the exponents α,β and z.
First, lets establish how time, space and the height functions scale in relation to

the exponents defined previously:

$$\vec{x}' = b\vec{x} \tag{3.2.21}$$

$$h' = b^{\alpha}h \tag{3.2.22}$$

$$t' = b^{z}t \tag{3.2.23}$$

where the primed terms are scaled and the non primed are the original expressions, the space being scaled by a factor b, consequentialy, height function and time are scaled by powers of b, consequentialy height function and time are also scaled by powers of b.
By chain rule, we obtain that the time derivative and the Laplacian scale as

$$\partial_{t'}h' = \frac{\partial b^{\alpha}h}{\partial t}\frac{\partial t}{\partial t'} = b^{\alpha-z}\partial_t h \tag{3.2.24}$$

$$\nabla'^2 h' = \frac{\partial^2 b^{\alpha}h}{\partial x_i^2}\frac{\partial^2 \vec{x}}{\partial x_i'^2} = b^{\alpha-2}\nabla^2 h \tag{3.2.25}$$

For the noise function we need to understand its units, and for this we will use the second moment,

$$\langle \eta^2 \rangle = D\delta^d(\vec{x})\delta(t) \tag{3.2.26}$$

$$\tag{3.2.27}$$

with d an integer equal to the number of the space dimension. If we apply (3.2.23) the second moment is

$$\langle \eta'^2 \rangle = D\delta^d(b\vec{x})\delta(b^z t) = Db^{-(z+d)}\delta^d(\vec{x})\delta(t) \tag{3.2.28}$$

Because the units of η are the same as $\langle \eta \rangle$, we can see that

$$\langle \eta \rangle = \sqrt{\langle \eta^2 \rangle} \sim b^{-\frac{(z+d)}{2}} \tag{3.2.29}$$

Finally, the re-scaled EW-equation is as follows

$$b^{\alpha-z}\partial_t h = b^{\alpha-2}\nabla^2 h + b^{-\frac{(z+d)}{2}}\eta \tag{3.2.30}$$

$$\Rightarrow \partial_t h = b^{z-2}\nabla^2 h + b^{\frac{z-d}{2}-\alpha} \tag{3.2.31}$$

Because the equation needs to be invariant under re-scaling, i.e. not dependent on b, we arrive at the following expressions for the exponents:

$$z = 2 \tag{3.2.32}$$

$$\alpha = \frac{2-d}{2} \tag{3.2.33}$$

$$\beta = \frac{\alpha}{z} = \frac{2-d}{4} \tag{3.2.34}$$

3.2.4 Kardar-Parisi-Zhang equation

The previous section presented us with the first equation to describe surface growth, the EW equation. In this section we are going to study the next big step in the mathematical analysis of surface growth, the Kardar-Parisi-Zhang equation or KPZ Kardar et al. (1986). Their work confronts the question of a system where deposition has no relaxation, that is, wherever a particle gets is where it stays. This brings a few problems, mainly the fact that now growth is **locally** normal to the surface giving surface growth a preferential direction which, at first glance, would brake the up-down symmetry we used to derive the EW equation. What effects could this bring to exponents values? Could the EW and KPZ equations belong to the same universality class? These questions will guide the section.

3.2.4.1 Constructing the KPZ equation

As we said in the introduction to the section, we are studying a deposition process with no relaxation; where the new particle lands it is where it stands. The immediate effect this has on surface evolution is the emergence of lateral growth since all growth will be, in an immediate vicinity to the landing point, perpendicular to the surface. This means that there is a driving force with a well established direction guiding the evolution of the profile, therefore we need to determine what will be the mathematical expression for said drive.
If we were to zoom into the surface and let a δt amount of time pass, we would see that the profile would have grown almost homogeneously, as figure 3.2.3 shows. Lateral growth can clearly be seen in this figure, in this case normal to the dashed tangent line.

What is the variation of the function height function h? Figure 3.2.3 clarifies this

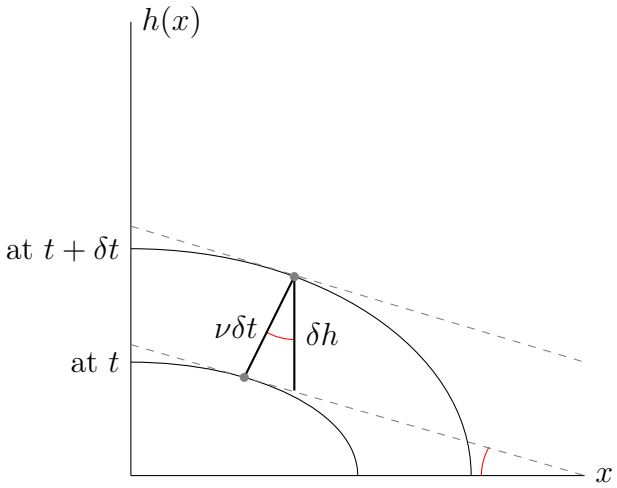

Figure 3.2.3: Local growth along the normal ν. This figure is important to understand the origin if the non linear term of the KPZ equation.

thanks to the Pythagorean theorem, we will have that

$$\delta h = \nu\delta t[(\nu\delta t)^2 + (\nu\delta t\nabla h)^2]^{\frac{1}{2}}, \tag{3.2.35}$$

where we can group by $\nu\delta t$, leading to the appearance of the non linear term $(\nabla h)^2$,

$$\delta h = \nu\delta t[1 + (\nabla h)^2]^{\frac{1}{2}}. \tag{3.2.36}$$

By considering small changes in the surface, that is to consider slopes much lower than one, therefore $|\nabla h| \ll 1$, the right hand side of equation (3.2.36) can be expanded as

$$\delta h = \nu\delta t[1 + \frac{(\nabla h)^2}{2} + \dots], \tag{3.2.37}$$

then we have found a new way if describing the temporal evolution of h as

$$\frac{\partial h(\vec{x}, t)}{\partial t} = \frac{\nu}{2} + \frac{\nu}{2}(\nabla h)^2 + \dots \tag{3.2.38}$$

With this result we can be sure that the term $(\nabla)^2$ is necessary to correctly describe any process of surface growth which admits laterla growth. Adding this to the EW equation, the model would be

$$\frac{\partial h(\vec{x}, t)}{\partial t} = \nu\nabla^2 h + \frac{\lambda}{2}(\nabla h)^2 + \eta(\vec{x}, t) \tag{3.2.39}$$

which is the KPZ equation. The addition of λ is to not lose genrality and is

interpreted as adding material for $\lambda > 1$, and removing material for $\lambda < 1$.
The main difference between the EW and KPZ equations comes from the symmetries they comply with. In section 3.2.2 we used symmetry arguments to build the EW equation, one of these symmetries being up-down symmetry, that is invariance under $h \to -h$ transformations. Moreover, in said section we ruled out terms of the type $(\nabla h)^{2n}$ since they break this symmetry.
Would this not mean that this symmetry is also broken by the KPZ equation? While is is true that a driving force in the system is a necessary condition to break up-down symmetry, as it would mean a preferential diection parallel to said force, it is not a sufficient condition as one could choose a coordinate system which follows the growth, and all symetries from the EW model would be preserve in this system.

3.2.4.2 Critical exponents in the KPZ model

We now face a critical question: What are the values for the critical exponents of the KPZ model? Following the steps from section 3.2.3, that is,

$$\vec{x}' = b\vec{x} \tag{3.2.40}$$

$$h' = b^{\alpha} h \tag{3.2.41}$$

$$t' = b^{z} t, \tag{3.2.42}$$

and apply the re-scaling to (3.2.39), then the scaled equation is

$$b^{\alpha - z}\frac{\partial h(\vec{x},t)}{\partial h} = \nu b^{\alpha-2}\nabla^2 h + \frac{\lambda}{2} b^{2\alpha-2}(\nabla h)^2 + b^{-\frac{d}{2}-\frac{z}{2}}\eta(\vec{x},t), \tag{3.2.43}$$

which multiplied by $b^{\alpha-z}$ is

$$\frac{\partial h(\vec{x},t)}{\partial h} = \nu b^{z-2}\nabla^2 h + \frac{\lambda}{2} b^{\alpha+z-2}(\nabla h)^2 + b^{-\frac{d}{2}+\frac{z}{2-\alpha}}\eta(\vec{x},t). \tag{3.2.44}$$

Naturally, this leads to a relation between α and z, since the non lineal term should be the same under scaling, hence

$$\alpha + z = 2, \tag{3.2.45}$$

condition which is valid for all dimensions since there is no dependence on d.
We said that by a correct selection of coordinate system, one could preserve all symmetries from the EW model in the moving KPZ model, meaning that they should be related. Then, how do we reconcile equation (3.2.45) with the exponents found in section 3.2.3?

3.2.4.3 Probability distributions in EW and KPZ models

Both EW and KPZ equations are Langevin equations of the sort

$$\frac{\partial h}{\partial t} = G(h) + \eta, \tag{3.2.46}$$

with η being Gaussian noise ($\langle \eta\eta' \rangle = 2D\delta(q - q')$), where we constructed the function G for each case.
Another way to approach this is to think about the probability of finding a profile or distribution of heights h at a time t, and so the question is, how does this probability density evolve? Luckily, we can count with the minds of the past to have thought of this question too, and the Fokker-Planck formalism is the right tool for the job.
All Langevin equations of the type in (3.2.46) admit representation as a Fokker-Planck equation as follows,

$$\frac{\partial \Pi(h,t)}{\partial t} = \frac{\partial}{\partial h}\left[-G(h,t) + D\frac{\partial}{\partial h}\right]\Pi(h,t), \tag{3.2.47}$$

where Π is the probability density function, in our case, the probability of having a profile h at time t.
Due to the fact that the height function h deppends on position $\vec{x}$, integration over the $\vec{x}$ of the right hand side is needed as h depends on the dimension of the space, therefore

$$\frac{\partial \Pi}{\partial t} = \int d^d\vec{x}\frac{\delta}{\delta h}\left[-G(h(\vec{x})) + D\frac{\delta}{\delta h(\vec{x})}\right]\Pi, \tag{3.2.48}$$

where $\delta/\delta h$ is the functional derivative.
First lets test the non-driven case, the EW equation. Equilibrium requires that

$$\frac{\partial \Pi_{\text{eq}}}{\partial t} = 0, \tag{3.2.49}$$

and by input of (3.2.20) we have that

$$\int d^d\vec{x}\frac{\delta}{\delta h}\left[-\nu\nabla^2 h(\vec{x}) + D\frac{\delta}{\delta h(\vec{x})}\right]\Pi_{\text{eq}} = 0, \tag{3.2.50}$$

which means that the integrand is to be equal to 0 at equilibrium,

$$\left[-\nu\nabla^2 h(\vec{x}) + D\frac{\delta}{\delta h(\vec{x})}\right]\Pi_{\text{eq}} = 0 \tag{3.2.51}$$

$$\Rightarrow \frac{\delta\Pi_{\text{eq}}}{\delta h(\vec{x})} = \Pi_{\text{eq}}\frac{\nu}{D}\nabla^2 h(\vec{x}). \tag{3.2.52}$$

This functional equation can be solved by assuming the functional form

$$\Pi_{\text{eq}} = e^{-\frac{\nu}{2D}\int d^d\vec{x}(\nabla h)^2}, \tag{3.2.53}$$

and by studying its variation with respect to δh we get that

$$\delta\Pi_{\text{eq}} = e^{-\frac{\nu}{2D}\int d^d\vec{x}(\nabla(h+\delta h))^2} \tag{3.2.54}$$

$$= \frac{\nu}{D}\Pi_{\text{eq}}\int d^d\vec{x}\delta h\nabla^2 h, \tag{3.2.55}$$

Now, the definition of a functional derivative, for a functional F with respect to a infinitesimal function $\delta f(x)$, is such that Parr and Weitao (1995)

$$\delta F = \int dx\frac{\delta F}{\delta f(x)}\delta f(x), \tag{3.2.56}$$

which for our case means that

$$\frac{\delta\Pi_{\text{eq}}}{\delta h(\vec{x})} = \Pi_{\text{eq}}\frac{\nu}{D}\nabla^2 h(\vec{x}), \tag{3.2.57}$$

and therefore the functional form (3.2.56) is correct.

For a $1-$dimensional profile we have that, as per equation (3.2.34), $\alpha = 1/2$ for the EW model, which is the equilibrium.

Now lets work the KPZ model, what would be the probability density distribution like?

The correspondant Fokke-Planck equation is

$$\frac{\partial\Pi}{\partial h} = \int d^d\vec{x}\frac{\delta}{\delta h}\left[-\nu\nabla^2 h(\vec{x}) - \frac{\lambda}{2}(\nabla h)^2 + D\frac{\delta}{\delta h(\vec{x})}\right]\Pi_{\text{eq}}, \tag{3.2.58}$$

for which there is no a priori stationary solution ($\partial_t \Pi = 0$). For $d = 1$, where the gradient reduces to a partial derivative of x, we do recover the functional form

$$\Pi = e^{-\int dx \frac{\nu}{2D}(\partial h)^2}, \tag{3.2.59}$$

which means that for the one dimensional case, the EW and KPZ model have the same equilibrium solution where the distributions of gradiaents follows a Gaussian distribution. Therefore, α is equal to $1/2$ for both the EW and one dimensional KPZ models, and using (3.2.45) we get that for the 1-d KPZ model

$$\alpha = \frac{1}{2}, \quad z = \frac{3}{2}, \quad \beta = \frac{1}{3} \tag{3.2.60}$$

3.2.4.4 Random walks and the KPZ model

A random walk is such that at any point in time there is an equal probability of $1/2$ for the walker to go up or down from the previous point, meaning that each step is independent from the one before it. Then, the probability to find the walker at a distance x from the starting point, at a time t is a Gaussian distribution with mean equal to zero, given that the starting point is the origin,

$$P(x,t) = \frac{1}{\sqrt{2\pi t}} \exp\left\{-\frac{x^2}{2t}\right\}. \tag{3.2.61}$$

In (3.2.61) it can be seen that the variance σ^2 is t, which means that the standard deviation follows

$$\sigma \propto t^{\frac{1}{2}} \tag{3.2.62}$$

$$\Rightarrow \langle [x(t_2) - x(t_1)]^2 \rangle^{\frac{1}{2}} \propto |t_2 - t_1|^{\frac{1}{2}}, \tag{3.2.63}$$

meaning that it scales as the square of the time interval. This is akin to increase the sample size for a surface, which leads to understanding that the profile generated by a random walk scales as $\sim L^\alpha$, with $\alpha = 1/2$.

With this in mind, it is intersting to study what is the distribution of slopes that form the profile described by the KPZ model, since if they follow a Gaussian distribution it would mean that both systems belong to the same universality class, equating their critical exponents. This is what we expected from (3.2.34), with $d = 1$, as it holds for all dimensions.

Chapter 4

Methodology

4.1 Synthesis of halide perovskite

For the synthesis of MA-PbI_3, a two step spin-casting method was applied where two solutions were used, one for Lead Iodide (PbI_2) and one for Methylammonium Iodide (MAI) over a $2[cm] \times 2[cm]$ fluorine-doped tin oxide (FTO) covered glass substrate. The compounds, quantity, concentration and provider for both solutions are shown in table 4.1.1 and 4.1.2, respectively. The spin-casting program had a duration of $90s$ in total, with an acceleration rate of $500RPM/s$ arriving at the top speed required. The first step is to drop the PbI_2 solution on the stationary substrate before starting the program to then start the spinning procedure. After $60s$ the MAI solution was dropped over the sample. Once spinning finished, the sample was annealed for 30 minutes at $100°C$ as shown in the diagram from figure 4.1.1. Following annealing, the sample was placed inside a closed petri dish and wrapped in aluminum foil over a plate heater at $30°C$ until being characterized.

Compound	**Quantity**	**Con.** $[mol/L]$	**Provider**
Lead Iodide	$0.461[g]$	1	Sigma Aldrich
Dimethyl Sulfoxide	$0.1[mL]$	1.4	Sigma Aldrich
Dimethylformamide	$0.9[mL]$	11.57	Merck

Table 4.1.1: Lead Iodide solution, aqueous volume of $1[mL]$.

The proportion between both solutions was PbI_2/MAI 0.8:1, being the exact amounts dropped over the substrate $80[\mu L]$ and $100[\mu L]$ due to the need to cover

Compound	Quantity	Con. $[mol/L]$	Provider
Methylammonium Iodide	0.065	0.31	GreatCellSolarMaterials
Isopropyl Alcohol	$1.3[mL]$	13	Sigma Aldrich

Table 4.1.2: Methylammonium Iodide solution, aqueous volume of $1.3[mL]$.

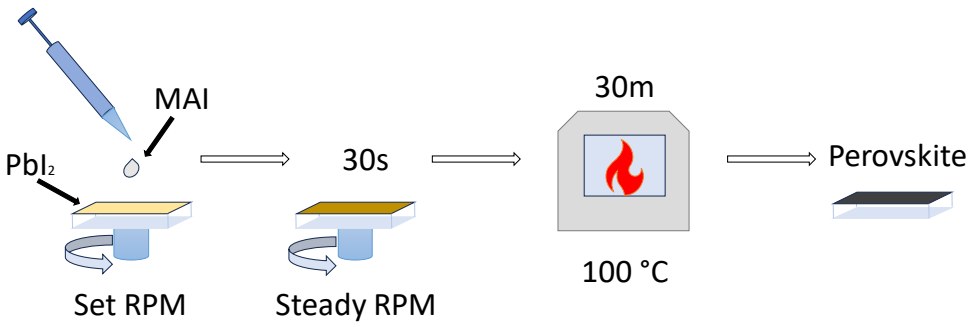

Figure 4.1.1: Diagram of the deposition method. First stage shows the substrate covered in PbI_2 solution (yellow), and while spinning the MAI being deposited, which turns the sample into a light brown. Second stage shows the two solutions over the spinning wafer, which then goes to the fourth stage of annealing and, in the final stage, the synthesized perovskite film.

the whole substrate.

Top spin velocity was the parameter being modified within the range of 600 and $1000RPM$, but samples cast at $1500RPM$ and $2000RPM$ were synthesized for comparison. Sadly, pictures of the process were not possible during synthesis, as contact with light and humidity are detrimental for the sample, each part of the process had to be quick and done in succession immediately one after the other. A picture of the final sample is shown in figure 4.1.2

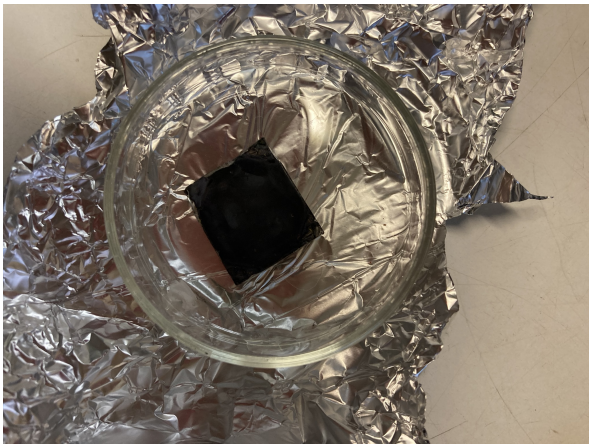

Figure 4.1.2: Final perovskite sample.

4.2 Atomic force microscopy

Atomic force microscopy or AFM is a surface characterization method which, in essence, consist of capturing height surface variations using a probe which is in contact with the surface. This probe consists of a tip mounted in a cantilever, where the tip whose width determines image resolution. There are two ways of probing the sample. The first one works by maintaining continuous contact with the sample, known as static force mode or contact mode, so that by moving the probe in straight lines around the surface, the cantilever deflects at each point where height changes, and these point to point deflections are then used to determine the height profile along the line. Think of it as sliding your finger tip in a surface, picking up the defects as your finger moves with them. How we capture the cantilever deflection is by pointing a laser to the end of it and receiving the reflection onto an photodiode, where the movement of the reflected ray from the center is what the computer converts to height data. A diagram of the system can be seen in figure 4.2.1.

The equipment used was the NaioAFM system from Nanosurf, shown in figure

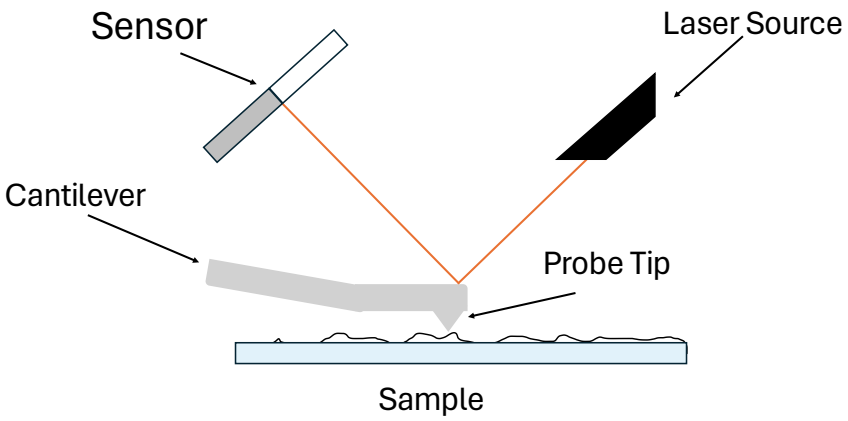

Figure 4.2.1: Schematic rendering of an AFM.

4.2.2, with the system supported on shock absorbing material blocks seen in the same image. The main sources of image noise were adjacent laboratories and construction nearby. The measurements were taken in low light conditions in order to preserve sample integrity, as shown in figure 4.2.3.

The AFM served two purposes:

- Imaging for morphological analysis

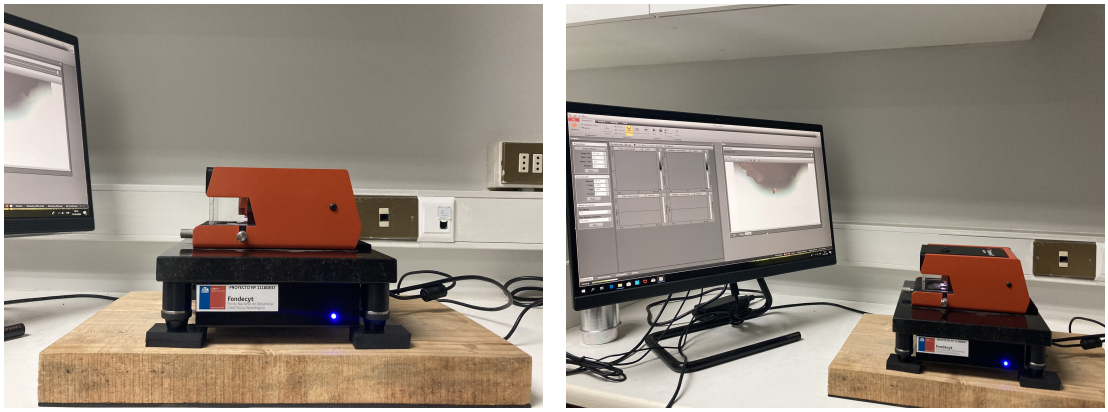

(a) **(b)**

Figure 4.2.2: Nanosurf NaioAFM system used in this work.

- Imaging for film thickness measurements

The second task is profilometry, which was done by scratching the surface of the sample with a scalpel, then aligning the cantilever with this line in order to measure from the clean line into the film.

Figure 4.2.3: Conditions for AFM characterization.

4.3 Autocorrelation function

A vital tool of statistical analysis is the **Correlation Function** or **Autocorrelation Function** (ACF), which mathematically is defined as

$$G(\vec{x},t) = \langle h(\vec{x},t)h(\vec{x}+\vec{r},t)\rangle \tag{4.3.1}$$

which gives us information of the similarity of height values at different distances, encoding information about roughness and correlation length. In order to find the correlation length using the ACF, we need to find the distance at which the function goes down to $1/e$ of the maximum value (arround 37% of the original value). It is assumed that the one-dimensional ACF will have the form of a Gaussian,

$$G_x(\tau_x) = \sigma^2 \exp\left\{-\left(\frac{\tau_x}{\xi}\right)\right\}, \tag{4.3.2}$$

where τ_x is the distance between points, σ is the RMS and ξ is the correlation length. Both of these methods can be applied.

This function is useful for non ordered formations since the self organization of the structures will occur locally at small scales compared to the sample size. Both of these methods can be applied.

An example of the ACF of a sample of $20 \times 20[\mu m]$ along with the one dimensional ACF is shown in figure 4.3.1.

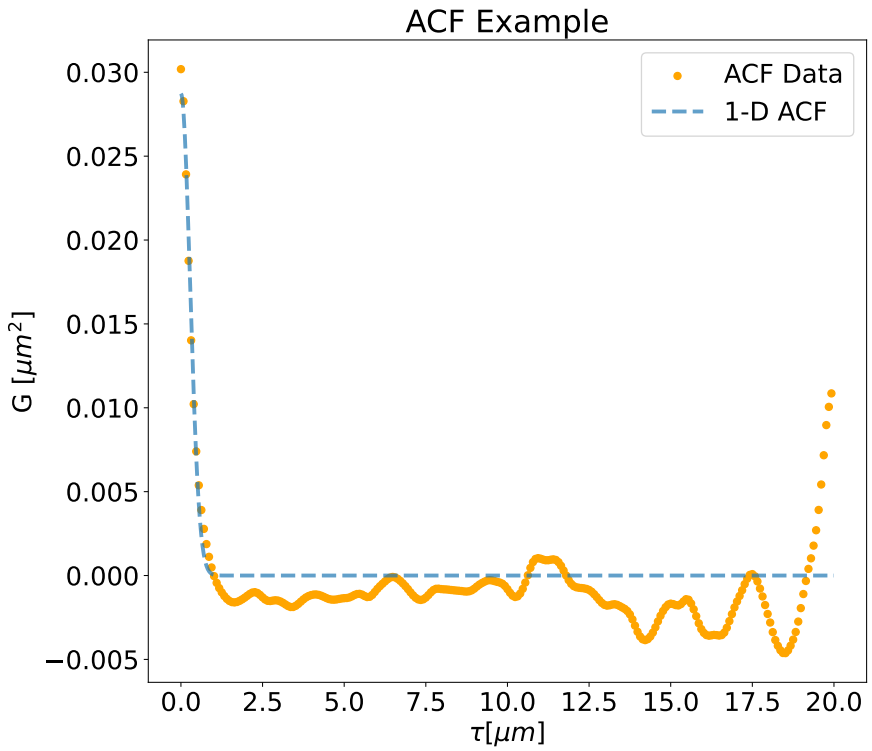

Figure 4.3.1: Example of how the ACF looks for one of the samples and the one-dimensional ACF Gaussian function as a dashed light blue line.

4.4 Height-height correlation function

In a similar fashion to the ACF, the **Height-Height Correlation Function** (HHCF) is a comparison of the height values at different points but instead of multiplication, we average over the height differences,

$$H(\vec{x},t) = \langle (h(\vec{x}+\vec{r},t) - h(\vec{x},t))^2 \rangle, \tag{4.4.1}$$

encompassing the information of RMS, correlation length and roughness exponent. How does this information appear in the function? This question is answered in the work by Sinha et al Sinha et al. (1988), where the because of assumed the Gaussian distribution of the random process the HHCF can written as a one-dimensional function

$$H_x(\tau_x) = 2\sigma^2[1 - \exp\left\{-\left(\frac{\tau_x^2}{\xi^2}\right)\right\}], \tag{4.4.2}$$

where τ_x is the distance between points, σ is the RMS and ξ is the correlation length.

This means that the function saturates after $\tau_x = \xi$, then we can say that the function has two segments,

$$H_x(\tau_x) \propto \begin{cases} \tau_x^{2\alpha} & , \tau_x < \xi \\ 2w^2 & , \tau_x > \xi \end{cases} \tag{4.4.3}$$

Figure presents 4.4.1 an example of the HHCF for one of our samples, showing the two branches of the HHCF and one-dimensional HHCF itself.

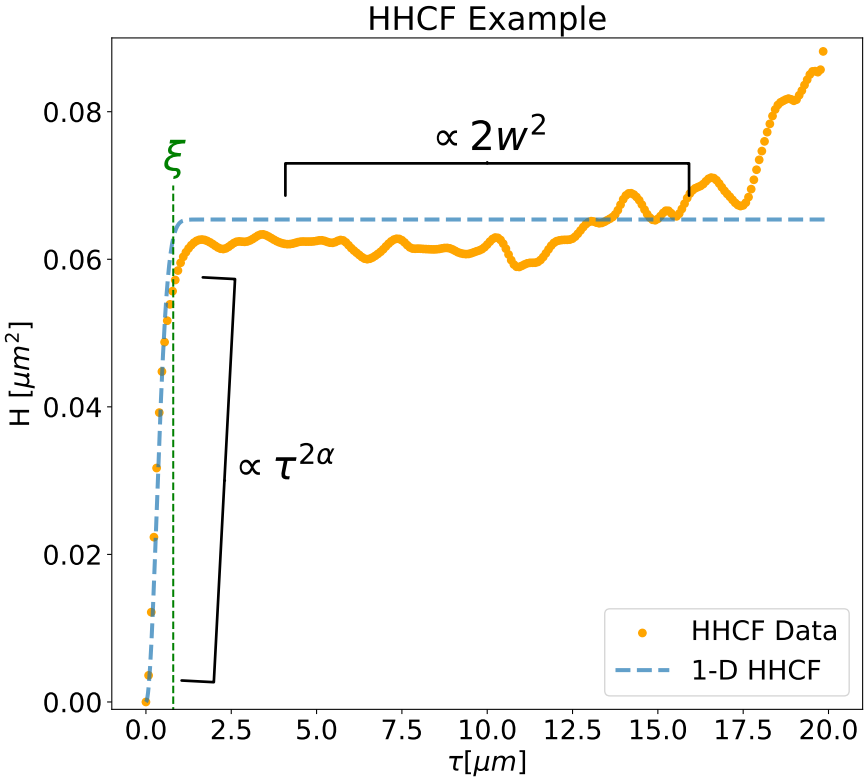

Figure 4.4.1: Example of how the HHCF looks for one of the samples and the one-dimensional HHCF Gaussian function as a dashed light blue line. The point where it saturates is the correlation length.

4.4.1 Power spectrum density (PSD)

Up to now we have worked with the real space being measured, that is, with a "photo" of the system. But when it comes to obtaining the exponents values it is useful to use the approach of Fourier analysis, in this case two dimensional Fourier transform. This approach makes finding information in a seemingly chaotic case by way of understanding the height profile as a sum of many patterns, organizing the information contained in the images we take of the sample as "how much energy of the system is contained in a given frequency". These frequencies have a wave lengths which are characteristic of each pattern, that is, lower frequencies correspond to longer patterns and high frequencies correspond to shorter patterns. In figure 4.4.2 we can see a standard PSD in which two distinct regions can be differentiated with both axis in log scale. The red dashed line denotes the dynamic region or correlated region and the blue line corresponds to the static region or uncorrelated region. What does this mean? If we consider that each frequency represents the characteristic length of a given pattern, we can understand that there should be a peak for a value of k in which correlation saturates and randomness characterizes the statistics of the system. Each value of α is characteristic of the growth mechanism which helps us understand the different stages of the sample.

Consider the structure factor in the Fourier space

$$S(\vec{k},t) = \langle h(\vec{k})h(-\vec{k},t)\rangle \tag{4.4.4}$$

where

$$h(\vec{k},t) = \frac{1}{L^{d/2}}\sum_{\vec{x}}(h(\vec{x},t)-\bar{h})e^{i\vec{k}\cdot\vec{x}} \tag{4.4.5}$$

By replacing (4.4.5) in (4.4.4) we obtain

$$S(\vec{k},t) = \langle\frac{1}{L^{d}}\sum_{\vec{x}}(h(\vec{x},t)-\bar{h})^2\rangle_{\vec{k}} \tag{4.4.6}$$

The mean operator is for a set value of $\vec{k}$, and if we observe the expression we can see that it is the expression for w in (3.2.2) squared. Further more, by adding for each value of $\vec{k}$ we get that

$$w^2(L,t) = \frac{1}{L^{d}}\sum_{\vec{k}} S(\vec{k},t) \tag{4.4.7}$$

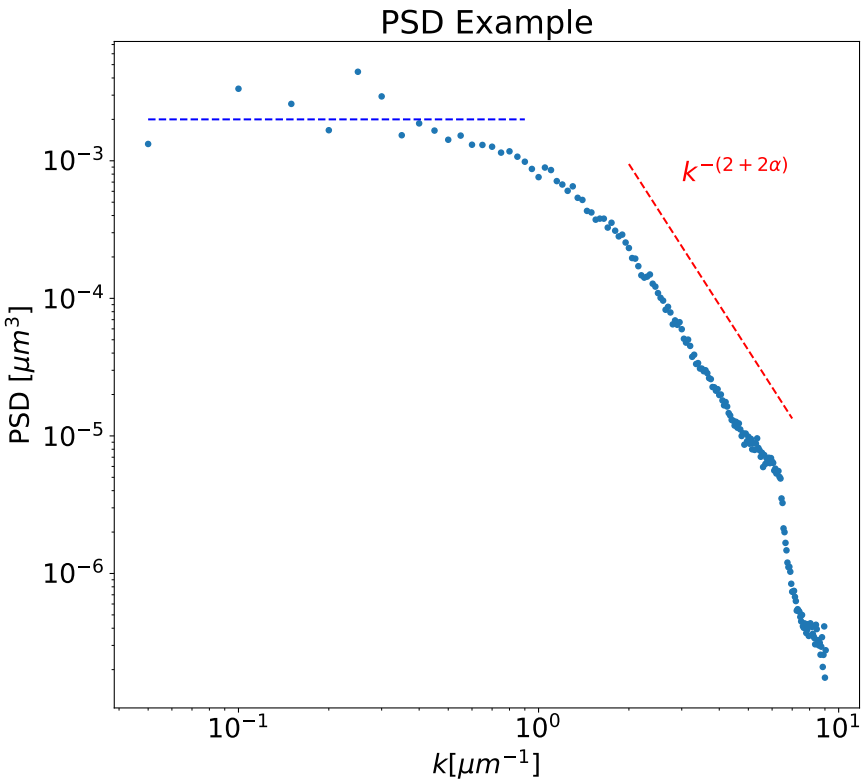

Figure 4.4.2: PSD example. In red the dynamic roughening part of the PSD, and in blue the saturation region.

On the other hand, we have the scaling relation (3.2.8) which, if we square it, tells us that

$$w^2(L,t) \sim L^{2\alpha} f\left(\frac{t}{L^z}\right)^2 \tag{4.4.8}$$

therefore, we can say that

$$S(\vec{k},t) \sim L^{d+2\alpha} \sim k^{-(d+2\alpha)} \tag{4.4.9}$$

Because in our case $d = 2$ we have that

$$S(\vec{k},t) \sim k^{-(2+2\alpha)} \tag{4.4.10}$$

This dominates the dynamic region in the PSD, letting us obtain α by fitting a function of the following nature

$$g(x) = Ak^{-(2+2\alpha)} \tag{4.4.11}$$

where A is an amplitude that modulates the fit.

4.5 X-Ray diffraction

We talked about how we can use the spectrum that comes from the diffraction pattern generated by a beam of X-ray interacting with a crystallized solid. In theory, these peaks should be discrete for each crystal plane but, as every good scientist knows, reality is always more complicated. Due to real solids having a certain thickness, the peaks will have width instead of being discrete lines, in general a Gaussian function suffices as representation of their shape. The width appears because the beam interacts not just with the two first layers of material, but with multiple bellow it, meaning that we need to consider the diffraction pattern generated by the whole.

For two sufficiently close incident ray angles, the path difference will be so that complete destruction interference will not occur. So for each peak there will be a distribution around the central peak where complete destructive interference is achieved at the bottom and upper limits of the distribution. This width decreases as crystal thickness increases since more reflected wave fronts are interacting, meaning that we could determine crystal size by analyzing the width of the peak. Yet again, reality is more complicated and, because a crystal will not be completely homogeneous, we are seeing effects not only of the thickness or size of the complete crystal but also of a substructure called crystallite.

Through this we arrive at Scherrer's equation Cullity (1956)

$$D = \frac{K\lambda}{B\cos\theta} \tag{4.5.1}$$

where D is the grain or crystallite size, K is the Scherrer constant, λ is the wavelength of the incident rays, B is the full width at medium height (FWMH) and θ is the angle at which the central peak occurs. The value used for K is 0.9 since this is the value for spherical crystallite.

The X-ray diffraction measurements were done at the GEA Institute of Universidad de Concepción. The equipment is a Bruker model D4 Endeavor X-ray Diffraction system with a LynxEye Detector, seen in figure 4.5.1. Measurement conditions were 10 to 70 degree 2θ with a step of 0.02 degrees and 0.4 second time step, divergence slit of $10[mm]$, and a copper radiation source anode with emission wavelength of $K\alpha = 0.15406[nm]$.

Figure 4.5.1: D4 Endeavor X-Ray diffraction system. Image sourced from Bruker (2024)

Chapter 5

Results & Analysis

5.1 Structure

The diffractogram (figure 5.1.2) shows the three diffraction patterns obtained for samples synthesized at 600, 1000 and 2000$[RPM]$. Since the common synthesis of lead halide perovskite is done at 2000$[RPM]$ and up, said sample is used as control to confirm the correct synthesis of the provskite.
From these difractograms we confirm the synthesis of tetragonal organic-inorganic hybrid lead perovskite Kumar et al. (2016), crystal structure shown in figure 5.1.1. The band structure in these structures has a band gap of $\sim 1.5[eV]$, making it a semi conductor which energy gap lies in the range of visible light. The effects of spin velocity on band gap are to be characterized in future. In section 3.1.8 the potential of a simple periodic array of protons was used to examplify how band

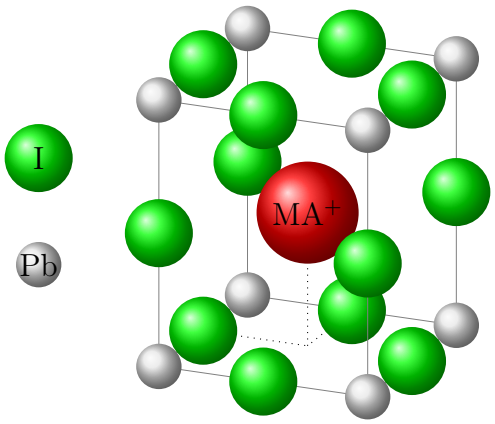

Figure 5.1.1: Tetragonal organic-inorganic hybrid lead perovskite structure.

structures form. For a more complex configuration, such as the structure in figure 5.1.1, will be vastly different. Moreover, small changes in structure could have great effects in band structure, and therefore in the value of the band gap.
The first two strong peaks correspond to the (002) and (110) planes, while the peaks at $\sim 28°$ and $\sim 31°$ correspond to the (202) and (310) planes respectively, both stable peaks across synthesis conditions. The peaks at $\sim 19°$ and $\sim 29°$, marked by the asteriks in figure 5.1.2, seem to correspond to the cubic phase of lead perovskite, which indicates that crystal structures is not homogeneous for the samples synthesized at lower speeds as they diminish in intensity for the higher spin speeds. This behavior is further studied in the work by Kumar et al. (2016).

Another factor to take into consideration is degradation as humidity greatly

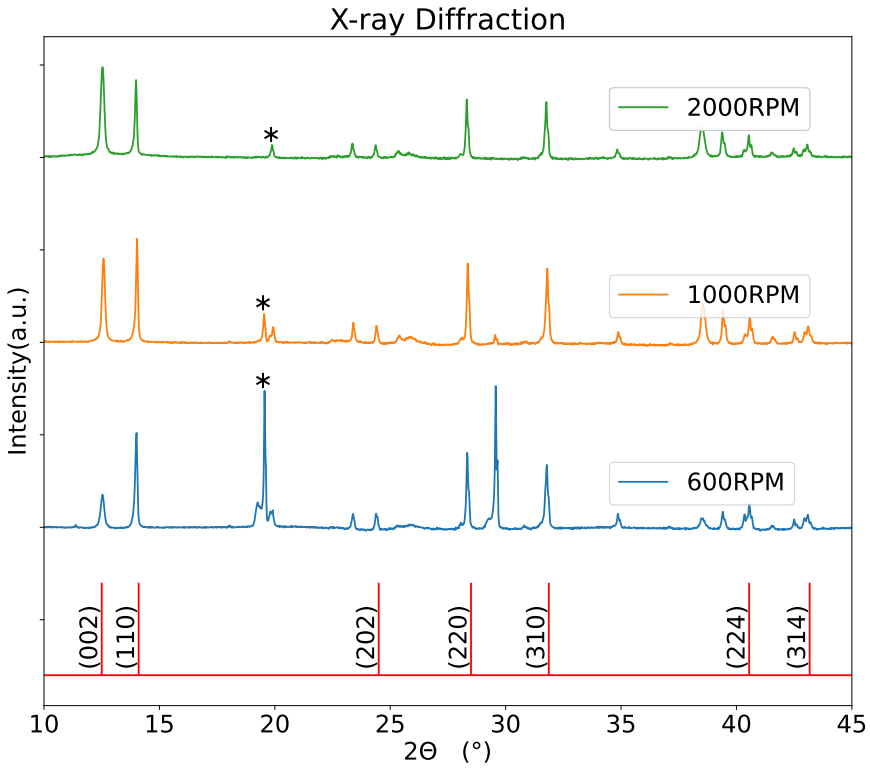

Figure 5.1.2: X-ray diffraction patterns corresponding to samples cast at 600 (blue), 1000 (orange) and 2000 $[RPM]$ (green). The peaks in red are the reported spectrum for tetragonal lead halide perovskite, and the asteriks denotes the peak at $\sim 19°$ for the cubic phase. The red line corresponds to the peaks in Kumar et al. (2016).

affects halide perovskite integrity, reducing it to PbI_2 Dhivyaprasath and Ashok (2023). This could be playing a factor in the cubic phase appearing for some samples as the synthesis was not under controlled condition, getting to 60%

humidity some days. We therefore confirm the synthesis of tetragonal lead halide perovskite with structural differences between synthesis conditions of spin casting velocities.

To determine crystallite size we use the (310) peak as is in the $30-50°$ and has a stable intensity. In figure 5.1.3 we present a zoom into the peak for each sample with a Gaussian fit with which we obtain the width at half height denoted as B, peak stability evident by it not moving from the 31.78° point.

As for the crystallite size, by using the Scherrer's equation we obtain the values

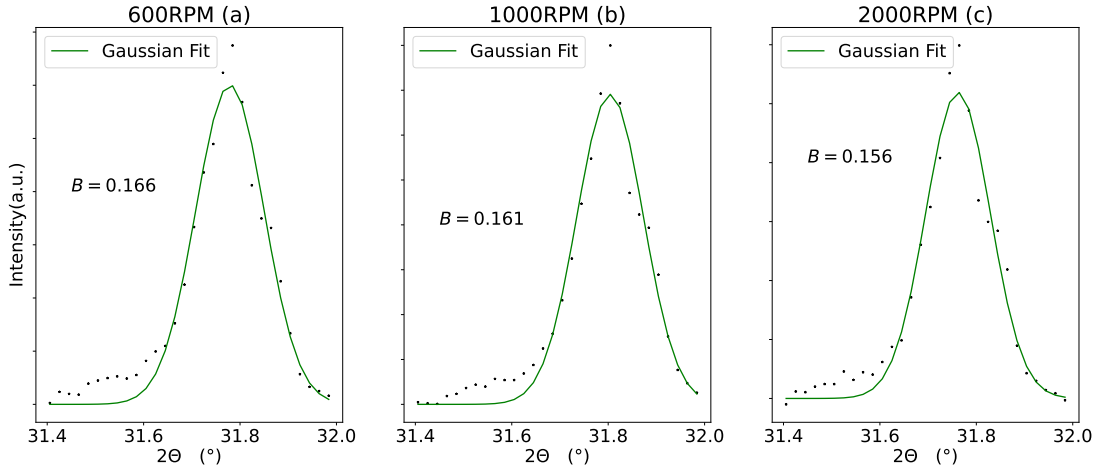

Figure 5.1.3: Peak (310) for the samples cast at (a) 600, (b) 1000, (c) 2000 $[RPM]$. The black dots correspond to the data while the green line is the gaussian fit from which we obtain the FWMH.

presented in table 5.1.1. Grain size has a slight increase from the 600$[RPM]$ to the 2000$[RPM]$ which can be explained by difference in film thickness to be discussed in the next section.

Spn.Vel. $[RPM]$	**Size**$[nm]$	$2\theta[°]$	**B**$[°]$
600	52	31.78	0.166
1000	53.5	31.80	0.161
2000	55.1	31.76	0.156

Table 5.1.1: FWMH and crystallite size by spin-casting velocity usimg the Scherrer equation.

5.2 Image Analysis

Images of $20 \times 20[\mu m^2]$, 512×512 pixels, 1 seconds per line, were taken via AFM for statistical analysis and profilometry. For statistical analysis, imaging was done by dividing the sample into four sectors, top right, top left, bottom rigth and bottom left. Imaging was done in the center of each sector, plus an image in the center of the sample, leaving a total of five images per synthesized sample. From all the synthesized samples the best were selected for analysis, the criteria being image noise and artifact presence. These images were treated using the image analysis program WSxM Horcas et al. (2007) by applying the flatten algorithm in order to offset the tilt present in the images. Then, in order to smooth the artifacts in the images, the image analysis program Gwyddion Nečas and Klapetek (2012) and its multiple line correction method was used a maximum of two times when required. The ACF and HHCF were also obtained from Gwyddion while the analysis of said functions was done using python scripts. In the case of RMS and correlation lenght, the values you see reported correspond to mean and standard deviation.

In the case of the computed critical exponents, because they arrise from the equations presented in section 3.2, they are the result of the fitting process done by custom programs written in python using the pandas, numpy and scipy libraries as well as personal scripts, meaning that that the reported values are the central value of the fit and the standard error.

Figure 5.2.1 shows an example for samples fabricated at 600, 700, 800, 900 and $1000[RPM]$, and the profiles corresponding to each of them are shown in 5.2.2. As the starting point of our analysis, we will visually describe the samples in order to see how structure size varies in relation to the spin-casting velocity. To this end, a representative image is presented for each case along side a graph of a profile line with the average height of said profile. Each image is $20 \times 20[\mu m^2]$.

Figure 5.2.1 **(a)** corresponds to a sample produced at $600[RPM]$, the structures being multiple columns tightly clustered creating something resembling a mountain chain.

A profile line with this bigger structure in the middle is shown in figure 5.2.2 **(a)**. It can be seen that this mountain is roughly $3[\mu m]$ wide at the base while the surroundings structures being more amorphous when it comes to defining a clear macro-structure.

If we compare image 5.2.1 **(a)** to the AFM image 5.2.1 **(b)** we notice a clear change in legibility. The sample synthesized at 700$[RPM]$ seems to not have prominent structures such as the mountain chain observed in the previous case. In contrast, we have many smaller tall mounts separated from each and can be more clearly observed if we refer to figure 5.2.2 **(b)** where we can see that these structures are more equally distributed along the length of the sample. More over, the average height goes down from the previous case from $\sim 1.4[\mu m]$ to $\sim 1[\mu m]$, as well as the maximum height measured. This can be explained by material availability since at lower speeds there is less material being removed from the wafer. As spin casting velocities increase we will see that this happens for all samples.

The sample fabricated at 800$[RPM]$, whose AFM image can be seen in figure 5.2.1 **(c)**, shows peak like structures as in the 700$[RPM]$ case, but the structures are more tightly packed and more evenly distributed. This can be more clearly observed in figure 5.2.2 **(c)** where peaks are seen in the profile line, and the widths at middle height that are around the $0.5[\mu m]$. Once again, the average height goes down to $\sim 0.69[\mu m]$ from the $\sim 1.5[\mu m]$ at 600$[RPM]$ and the $\sim 1[\mu m]$ at 700$[RPM]$. We will see how roughness changes in the next section to better understand the growth process.

With the 900$[RPM]$ sample, the downward trend for the average height continues, as can be seen in the profile line from figure 5.2.2 **(d)**, reaching the $\sim 0.51[\mu m]$, but differently from the 800$[RPM]$ sample, elevated lines can be appreciated that seem to be randomly distributed as seen in figure 5.2.1 **(d)**. These could be a result from formations similar to the one observe in the case of the 600$[RPM]$ sample, all be it smaller in width and height. The broad peak in 5.2.2 **(d)** corresponds to one of these structures diagonal cross section, leading to what seems like a wider base.

Lastly, the sample synthesized at 1000$[RPM]$, seen in figure 5.2.1 **(e)**, shows the tightly packed peaks previously seen in the 800$[RPM]$ sample also corroborated in the line profile, seen in figure 5.2.2 **(e)**. Once again, the average height decreases arriving at $\sim 0.34[\mu m]$ with no strong effects on the width at medium height of the structures.

These profile lines serve the purpose of understanding the structures in the film, but not film thickness as there is no a reference point with no material on top of the

substrate, therefore the information we obtain from these profiles is representative just of the structures. The results for film thickness via profilometry are presented in the next section.

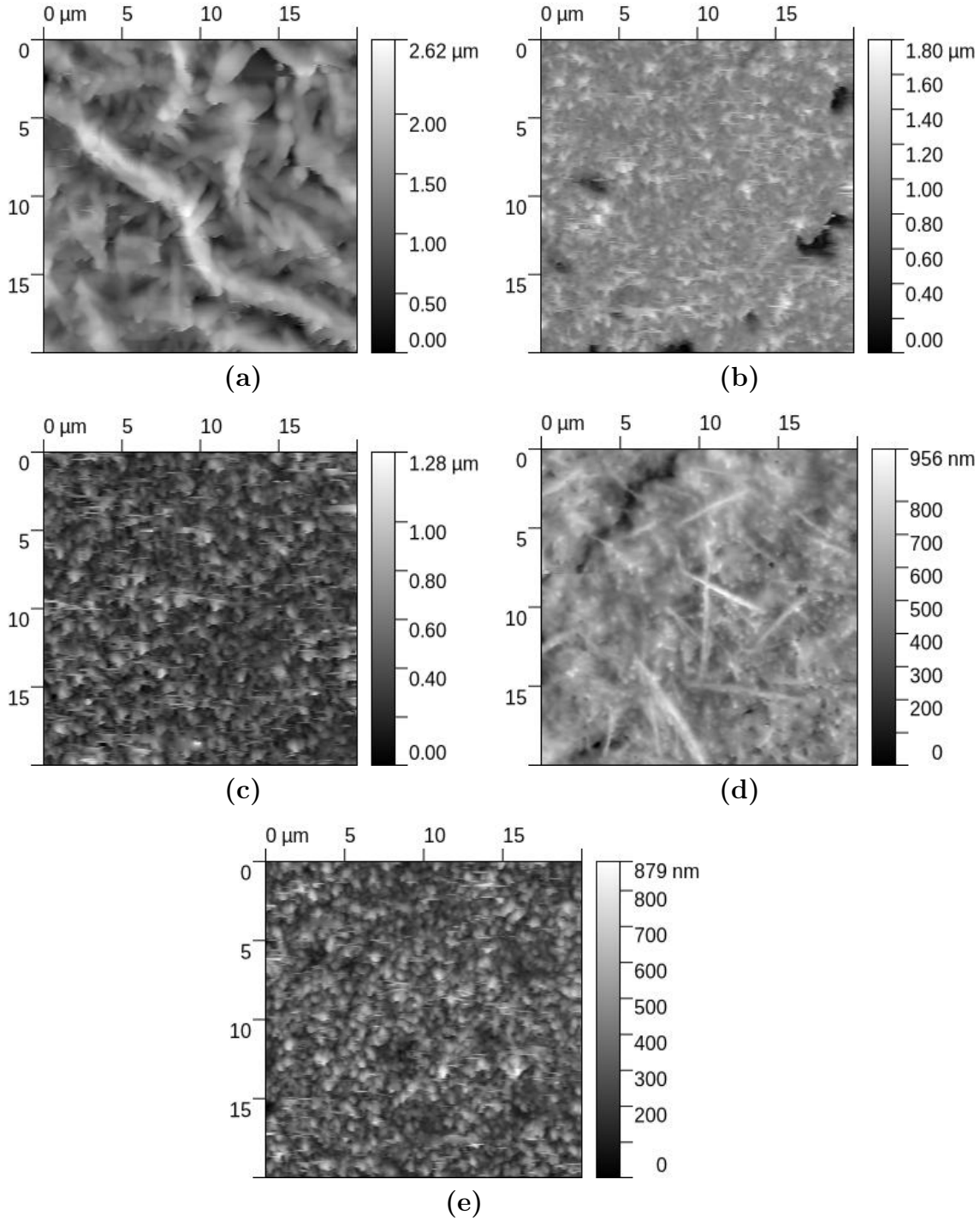

Figure 5.2.1: AFM images of samples synthesized at **(a)** 600, **(b)** 700, **(c)** 800, **(d)** 900 and **(e)** 1000 [RPM].

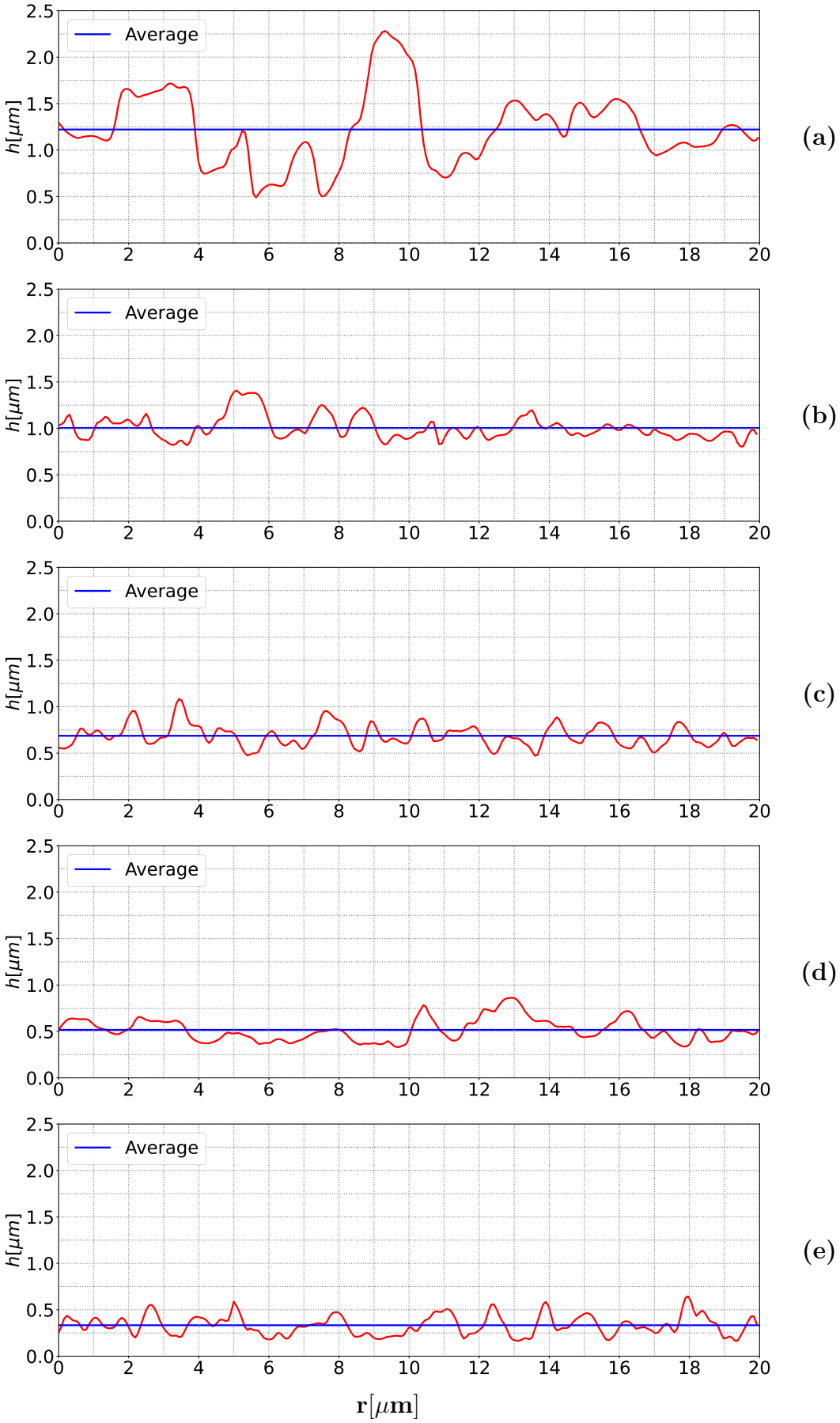

Figure 5.2.2: Profiles (in red) and averages (in blue),from samples synthesized at **(a)** 600, **(b)** 700, **(c)** 800, **(d)** 900 and **(e)** 1000 $[RPM]$.

5.3 Film Thickness

Film thickness was obtained via profilometry, results which are shown in figure 5.3.1. The region from 600 to 1000$[RPM]$ presents an stable relation between spin velocity and film thickness, depicted by the linear fit in blue and the fit being $D[\mu m] = (-5.7 * 10^{-4} \pm 5 * 10^{-5})v + 6.6 * 10^{-1} \pm 4 * 10^{-2}$, D being film thickness and v the spin velocity, which will be our **region of interest**. The obtained values for thickness are summarized in table 5.3.1 for a more precise reading of the results. We had expected film thickness decreasing with increasing spin velocity,

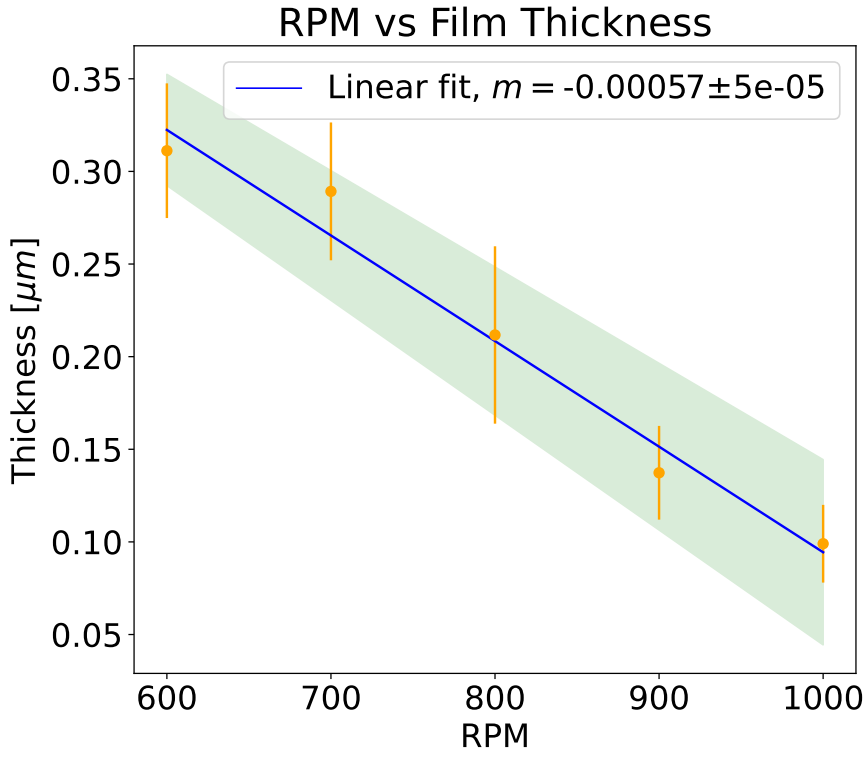

Figure 5.3.1: Film thickens (orange) by spin ACF-casting velocity. The fit (blue) with the first confidence interval for the slope in green demonstrating the linear relation between spin and thickness.

and this is confirmed by the results of table 5.3.1 where the maximum thickness was achieved by the 600$[RPM]$ synthesis, with an average value of 0.3$[\mu m]$, and the lowest thickness being that of the 900$[RPM]$ sample at 0.097$[\mu m]$, meaning that there was a variation of 0.067$[\mu m]$ in the spin velocity regime of interest. This is very fruitful for our approach as we postulate that spin velocity can be used instead of deposition time for the subsequent analysis since both have a direct effect on film thickness, greater deposition times being related to lowers

spin casting velocities and vice versa.

Spn.Vel. $[RPM]$	**Thickness** $[\mu m]$
600	0.31 ± 0.05
700	0.29 ± 0.05
800	0.21 ± 0.07
900	0.13 ± 0.03
1000	0.10 ± 0.02

Table 5.3.1: Film thickness by spin-casting velocity.

5.4 Roughness and growth exponent

The AFM images obtained are a height map of the sample as we have established, and so it is finally the moment for the statistical tools presented in chapter 3.2 to shine. Following the train of thought presented in said chapter, the first piece of information that we need in order to construct a coherent analysis is the surface roughness. To this end we are going to use two methods,

- Use the statistical information given by the image analysis program WSxM Horcas et al. (2007)
- Use the Height-Height correlation function

With the RMS and thickness values in our hands we can determine the growth exponent as per our hypothesis, which is the exponent characterizing how the roughness evolves before saturation.
Starting with the first method, film roughness went steadily down from $0.15[\mu m]$ at $600[RPM]$ to $0.137[\mu m]$ at $900[RPM]$ (table 5.4.1) to then jump to $0.16[\mu m]$ for the $1000[RPM]$ sample. We can see the relation between roughness and film thickness in figure 5.4.1, where there is a region between the before mentioned 600 and $900[RPM]$ with steady increase of RMS. Here, by fitting an exponential function we can compute the growth exponent, whose value for our case is $\beta = 0.09 \pm 0.09$. The growth exponent characterizes roughness time evolution meaning that the region of interest presents a steady growth, therefore the tools of dynamic scaling theory can be used in order to determine if the system is self affine.

Spn.Vel. $[RPM]$	**RMS**$[\mu m]$ **WSxM**	**RMS**$[\mu m]$ **HHCF**
600	0.152 ± 0.009	0.179 ± 0.01
700	0.146 ± 0.004	0.163 ± 0.008
800	0.143 ± 0.005	0.152 ± 0.009
900	0.137 ± 0.002	0.11 ± 0.01
1000	0.163 ± 0.003	0.18 ± 0.02

Table 5.4.1: Roughness by spin-casting velocity.

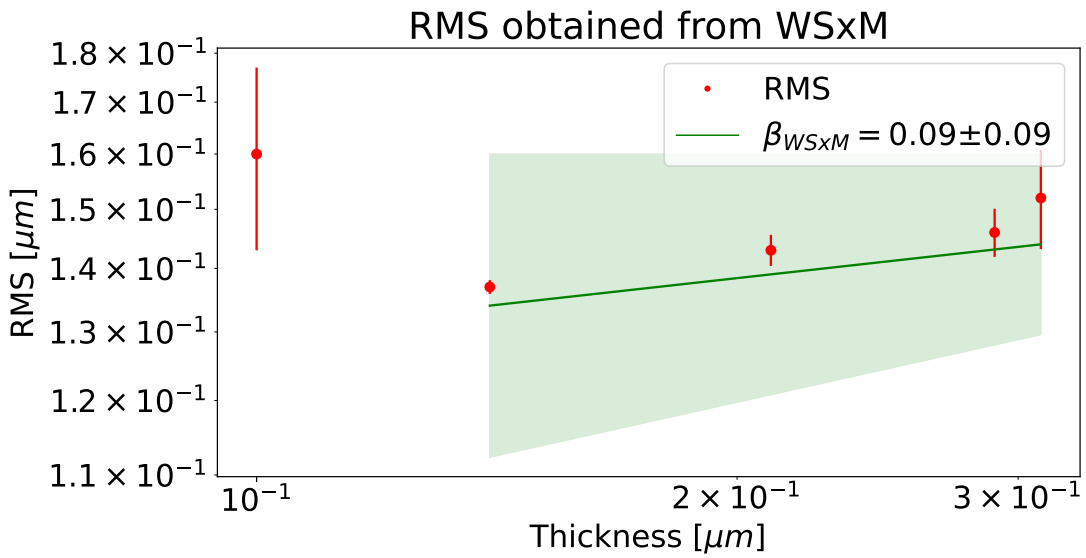

Figure 5.4.1: Plot of RMS obtained for each AFM image, average and standard error in red. The fit in green gives us a growth exponent of $\beta = 0.09 \pm 0.09$ with the confidence interval plotted in green.

Continuing with the second method, figure 5.4.2 shows the HHCF plot for one sample fabricated at each different spin-casting velocity. We can see very similar behavior when it comes to roughness trend across the various spin-casting velocities.

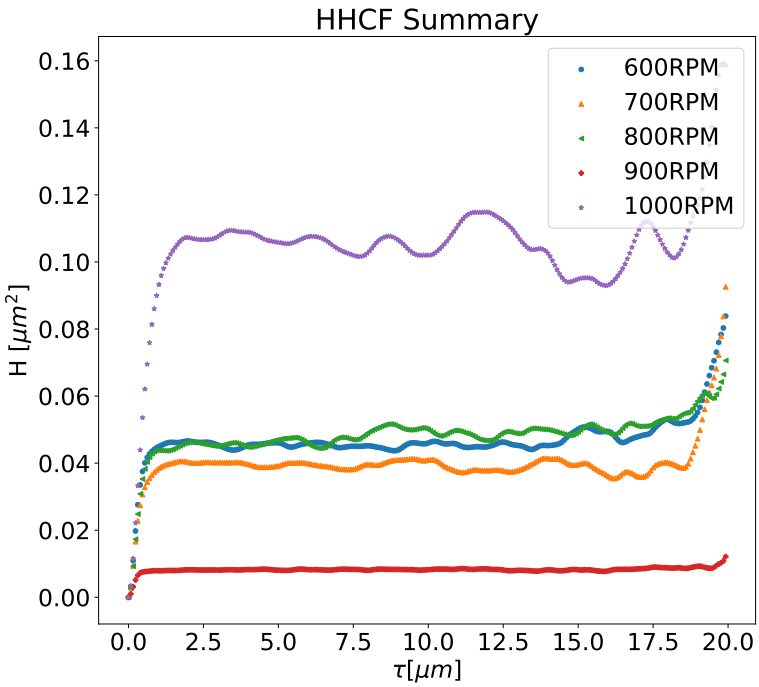

Figure 5.4.2: Summary of the HHCF per spin-casting velocity, one sample per speed.

In table 5.4.1, we can see that from 600$[RPM]$ to 900$[RPM]$ there is a clear decline just as in the values derived from the previous method, from 0.179$[\mu m]$ at 600$[RPM]$ to 0.11$[\mu m]$ at 900$[RPM]$, to the jump up to 0.18$[\mu m]$ at 1000$[RPM]$. The differences in RMS between methods are enough that the growth exponent we calculate from these roughness values is $\beta = 0.3 \pm 0.2$, shown in figure 5.4.3, compared to the previous 0.09. It is also easier to see how the overall trends of RMS in relation to film thickness are similar between the two ways of roughness determination, where there is a steady growth region for the samples fabricated between 600 and 900$[RPM]$.

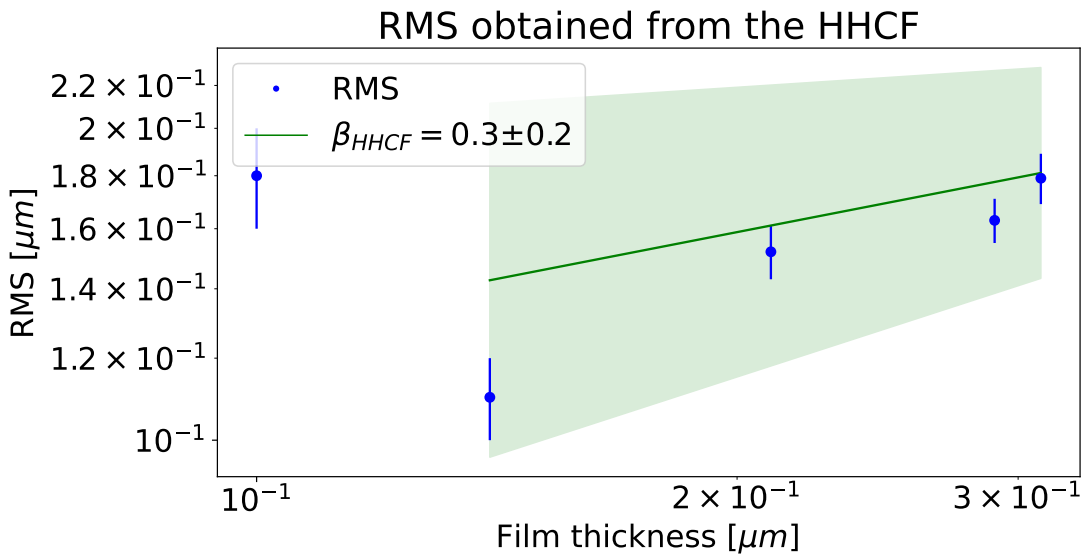

Figure 5.4.3: Plot of RMS obtained for each AFM image, average and standard error in blue. The fit in green gives us a growth exponent of $\beta = 0.3 \pm 0.2$ with the confidence interval plotted in green.

5.5 Correlation length an dynamic exponent

The next step in our analysis is to find the correlation length ξ of the different samples, see how does the system organizes in relation to the spin-casting velocity. As in the previous section there are two tools at our disposal, them being the HHCF once again and the ACF. Both these function are similar in the algorithmic side but test for different things, the HHCF probing the squared difference between heights at different distances, while the ACF works with the multiplication of these heights. Figures 5.5.1 and 5.4.2 present the ACF and HHCF respectively, one plot for each spin-casting velocity.

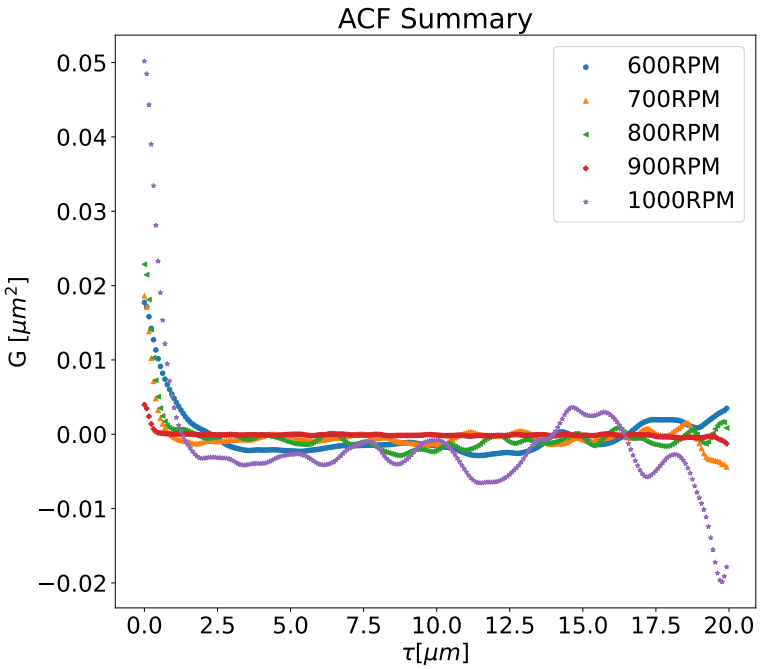

Figure 5.5.1: Summary of the ACF per spin-casting velocity, one sample per speed.

Table 5.5.1 shows the correlation lengths from the ACF and HHCF. In both cases we see a decrease in ξ value between 600 and 900$[RPM]$, to the increase at 1000$[RPM]$. The main difference is seen at 600$[RPM]$, where the correlation length calculated using the ACF is 0.87$[\mu m]$ compared to the 0.67$[\mu m]$ obtained via HHCF, and while ξ value is also different for the other cases, the biggest discrepancy is this first one.

Plotting ξ versus film thickness not also helps with visualization, but it is also the

Spn.Vel. $[RPM]$	$\xi[\mu m]$ **ACF**	$\xi[\mu m]$ **HHCF**
600	0.87 ± 0.05	0.67 ± 0.08
700	0.52 ± 0.05	0.48 ± 0.04
800	0.45 ± 0.04	0.41 ± 0.03
900	0.44 ± 0.08	0.36 ± 0.03
1000	0.46 ± 0.03	0.41 ± 0.03

Table 5.5.1: RPM and correlation length given by the ACF and HHCF.

next step in the application of dynamic scaling theory, since we use film thickness instead of deposition time. With these graph we can obtain the dynamic exponent z which characterizes at what time the system reaches roughness saturation. This will be vital to determine what type of system we are studying by its universality class.

Figures 5.5.2 and 5.5.3 correspond to the previously mentioned plots, with their respective $\propto t^{1/z}$ fits and z values, using the ACF and HHF ξ values.

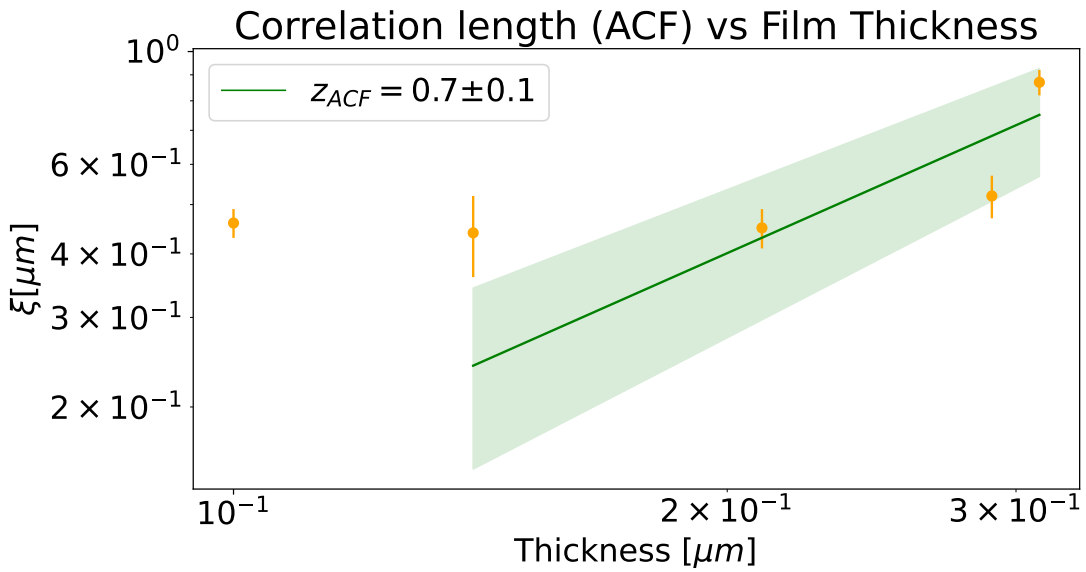

Figure 5.5.2: Average correlation length and standard error in orange vs film thickness. Exponential fit in green yields a dynamic exponent of $z = 0.7$.

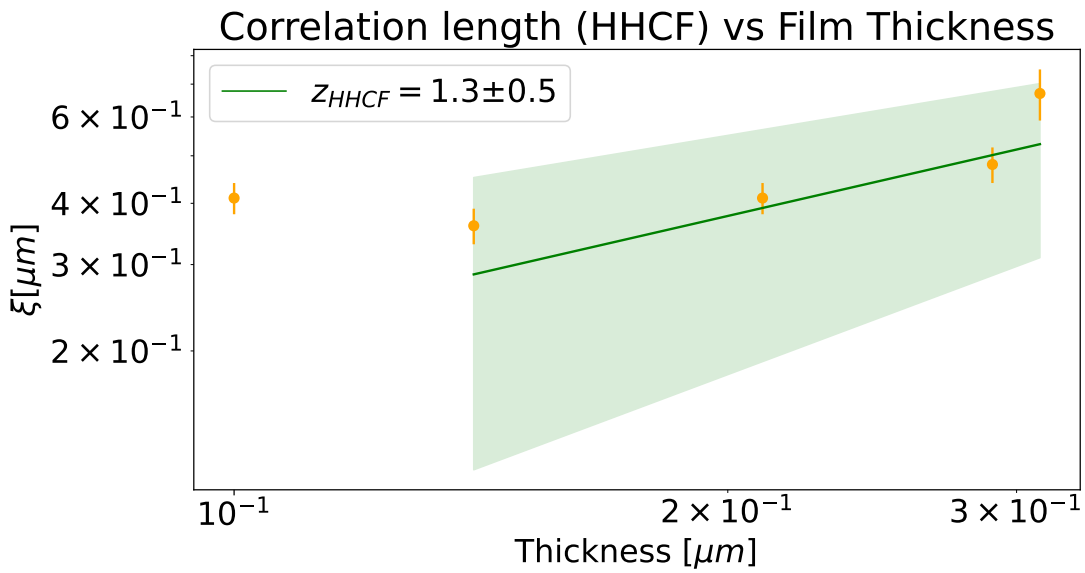

Figure 5.5.3: Average correlation length and standard error in orange vs film thickness. Exponential fit in green yields a dynamic exponent of $z = 1.3$ in green.

It is interesting to notice how both cases have broadly the same tendencies, where ξ stays more or less stable until a sharp rise at $600[RPM]$ and how the magnitude of these rise completely changes the value of the dynamic exponent.

5.6 Roughness Exponent

The growth exponent α characterizes how the saturation with scales width sample size, meaning that it gives us an understanding of how the roughness of a sample (standard deviation of a random process) changes as we increase or decrease the sample size. To this end we have three methods to be used:

- By using the scaling condition (3.2.8)
- By way of the HHCF
- By analyzing the power spectrum density (PSD)

On the scaling relation case we have two possibilities which relate to the previous two exponent, that is to use the growth and dynamic exponents we calculated with the HHCF, and the growth exponent derived from the WSxM rms values in combination with the dynamic exponent computed from ξ values of the ACF. This yields two numbers, $\alpha_{\beta z,HHCF} = 0.4 \pm 0.3$ and $\alpha_{\beta z,ACF} = 0.06 \pm 0.06$, where the former is greatly affected by the standard error of the dynamic exponent and the later having zero as a plausible value because of the growth exponent.
The second way to obtain α is to use the saturated region of the HHCF where the function is proportional to the squared roughness, $\propto w^2$, which yields $\alpha_{HHCF} = 0.72 \pm 0.04$. The summary of the plots is in figure 5.4.2.
Continuing with the final method, we know that the PSD gives us information about how much power is contained in a given frequency, so understanding what this frequency is for the system is the key, in our case it is the length of the patterns or modes that conform the sample's landscape, with the lower frequencies being the longest reaching modes and the higher frequencies being the the shorter ones, there fore, the amplitude reveals to us how much is each mode contributing to surface roughness. Now, recalling the dependency on alpha for the PSD in the dynamic region, $k^{-(2+2\alpha)}$, we can understand that α modulates the contributions to roughness by mode length, behavior called kinetic roughening.
A summary of the PDSs is shown in figure 5.6.1 with one sample per RPM. In this graph it can be seen that no peaks are present meaning that no periodic structure was found, and that there is a clear region of dynamic roughening in the high frequencies. The specific values are shown in table 5.6.1, with the mean α in the region of interest being $\alpha_{PSD} = 0.53 \pm 0.09$.

Spn.Vel. $[RPM]$	α **(average)**
600	0.51 ± 0.08
700	0.5 ± 0.1
800	0.59 ± 0.08
900	0.5 ± 0.1
1000	0.62 ± 0.09

Table 5.6.1: Roughness exponent by spin-casting velocity.

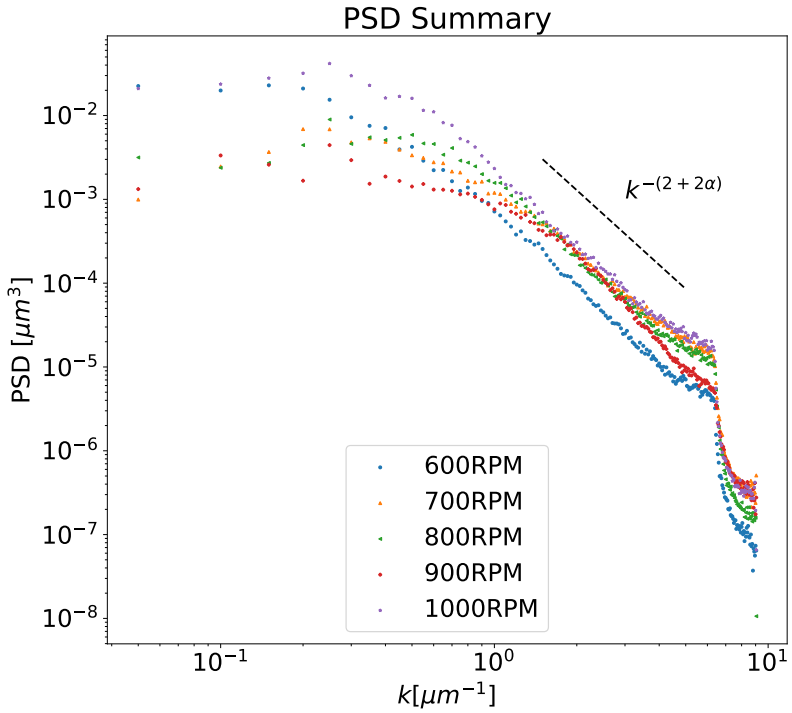

Figure 5.6.1: PSD of samples cast at the different RPMs. The average roughness exponent in the region of interest is $\alpha = 0.53$.

We can now compare these numbers and, to aid with visualization and comprehension, you can see a graphical comparison in figure 5.6.2. First, it is important to note that no value is close to 1, meaning that no anomalous growth is observed. Secondly, the direct α_{HHCF} differs from the exponent obtained by the scaling relation, $\alpha_{\beta z,HHCF}$, a difference of $\alpha_{HHCF} = \alpha_{\beta z,HHCF} + 0.32$, which is not unheard of Parveen et al. (2020), and due to the validity intervals of both values, there is the possibility that $\alpha_{HHCF} \approx \alpha_{\beta z,HHCF}$.
None of the values are exactly equal to another, with $\alpha_{\beta z,ACF}$ the furthest from the rest possibly reaching 0. We can consider that the realm of possibilities make it

so that $\alpha_{\beta z,HHCF} \approx \alpha_{PSD}$ which would tell us that the system follows the scaling law, therefore the Family-Vicsek equation could properly describe the system.

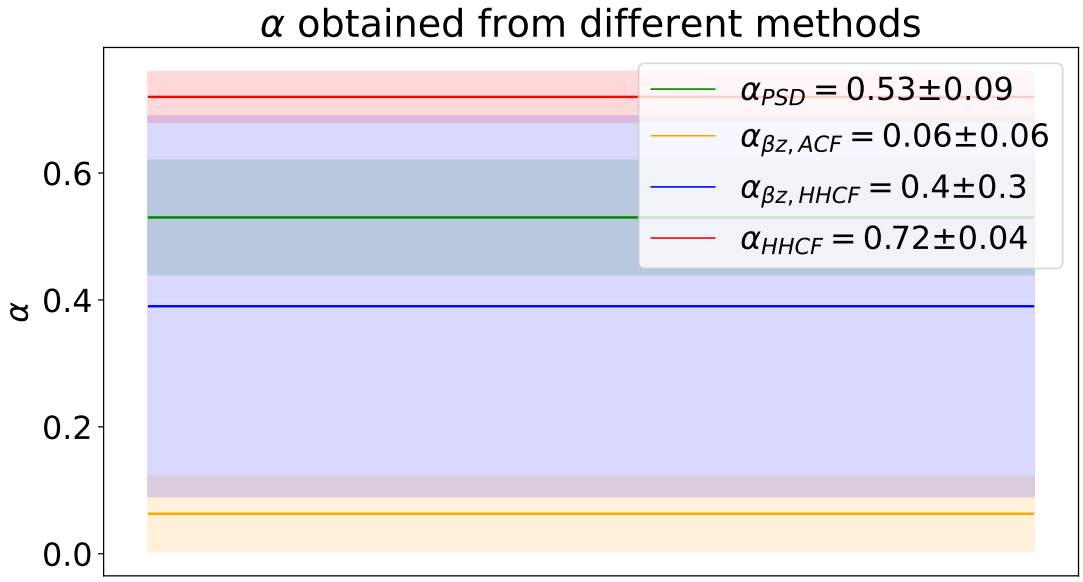

Figure 5.6.2: Roughness exponent obtained via PSD analysis in green, scaling relation from ACF and HHCF in orange and blue respectively, and directly from the HHCF in red.

The values of the growth, dynamic and roughness exponent come very close to the exponents of a one dimensional KPZ system where $\alpha = 0.5$, $z = 1.5$ and $\beta = 0.\bar{3}$ (see 3.2.4). This would mean that in the range between 600 and 1000$[RPM]$, lead halide perovskite distributes and grows as does a one dimensional profile with lateral growth, that is, grows as waves following the the local normal direction of the height function.

Chapter 6

Conclusions

Thin film lead halide perovskite were successfully synthesized under spin-casting velocities 600 $RPM, 700$ $RPM, 800$ $RPM, 900$ RPM and 1000 RPM, confirmed by X-ray diffraction characterization. Grain size changed between samples increasing with RPM. A mixture of cubic and tetragonal phase was observed as the peak near $2\theta = 19°$ indicates, being more prevalent for the $600RPM$ sample while tetragonal phase dominated for samples synthesized at higher velocities.

Their morphology were studied via atomic force microscopy and using the theoretical framework of dynamic scaling theory. We find that spin-casting velocity and thickness were inversely proportional in the region between 600 and 1000$[RPM]$, which we call our region of interest, proven by the negative slope of the linear fit $-5.7 * 10^{-4}$, which means that spin speed can be used as a proxy parameter for deposition time expanding the use of these analysis tools to systems where material dispersion is achieved by spin-casting.

Different methods of statistical analysis were used and compared, them being the Height-Height Correlation Function, Auto Correlation Function and the Power Spectrum Density.

Roughness evolution with thickness yielded two growth exponents, $\beta_{WSxM} = 0.09 \pm 0.09$ and $\beta_{HHCF} = 0.3 \pm 0.2$, and by comparing thickness to correlation length we find two dynamic exponents, $z_{ACF} = 0.7 \pm 0.1$ and $z_{HHCF} = 1.3 \pm 0.5$. These values yield the calculated roughness exponent $\alpha_{\beta z,ACF} = 0.06 \pm 0.006$ and $\alpha_{\beta z,HHCF} = 0.4 \pm 0.3$.

Direct analysis of the HHCF also gave a roughness exponent of $\alpha_{HHCF} =$

0.72 ± 0.004, meaning that there could be a deviation from the scaling law given by $\alpha_{HHCF} = \alpha_{\beta z,HHCF} + 0.32$.
The power spectrum densities of each samples were analyzed finding no periodic structures as no peaks were found. The linear region of the PSD reveals a roughness exponent of $\alpha = 0.53 \pm 0.09$ in the region of interest, which for the possible cases for both PSD and calculated $\alpha_{\beta z,HHCF}$ means that the system obeys the Family-Vicsek scaling relation confirming that the system is self affine.
Film thickness is a viable variable to use instead of deposition time, which means that dynamic scaling theory is usable for processes that do not use random deposition of material.

6.1 Limitations

The limitations we encountered had relation to two main factors: sample decay and vibration noise. Lead halide perovskite is highly sensitive to humidity, as it degenerates into PbI_2 when in contact with water, and the facilities where we operate have no enviromental control. Furthermore, Concepción where the laboratory is located has humidity usualy on the lines of 60%, making sample preservation a difficult task.
Lead perovskite also degrates under light contact, which made AFM imaging a task against time, as the light from the optical camera degraded the sample over the imaging process.
To this end we found that keeping the samplet encased in a petri dish, covered in aluminium foil at $30°C$ was optimal for preservation, but once AFM imaging was done the sample was no longer usable for other type of characterization techniques.
When it comes to image noise, the main contributors where construction projects nearby as in inside the building. Shock absorbing material prove to be sufficient for quality imaging.
Material availability also became an issue as it was necessary to decide what characterizations to do, which made the non reusable nature of the samples a problem. Just one technique could be done by sample.

6.2 Future work

Opto-electric characterization will be important in order to understand how these morphological changes affect electron reabsortion, as thickness increease would make it so that electron free path becomse smalle and smaller compared with the film. As perovskite is to be used in solar cells, it is crucial to understand this. Effects on band gap are also to be studied, as changes in crystallite size could greatly affect the absorbtion spectrum of the material.

Bibliography

Bloch, F. (1928). Quantum mechanics of electrons in crystal lattices. *Z. Phys*, 52:555–600.

Bruker (2024). *D4 Endeavor*. https://www.brukersupport.com/ProductDetail/732 [Accessed: Whenever].

Chapin, D. M., Fuller, C. S., Pearson, G. L., et al. (1954). A new silicon p-n junction photocell for converting solar radiation into electrical power. *Journal of applied physics*, 25(5):676.

Cui, J., Yuan, H., Li, J., Xu, X., Shen, Y., Lin, H., and Wang, M. (2015). Recent progress in efficient hybrid lead halide perovskite solar cells. *Science and technology of advanced materials*, 16(3):036004.

Cullity, B. D. (1956). *Elements of X-ray Diffraction*. Addison-Wesley Publishing.

Dhivyaprasath, K. and Ashok, M. (2023). Degradation behavior of methylammonium lead iodide (ch3nh3pbi3) perovskite film in ambient atmosphere and device. *Solar Energy*, 255:89–98.

Einstein, A. (1905). Über einen die erzeugung und verwandlung des lichtes betreffenden heuristischen gesichtspunkt.

Green, M., Dunlop, E., Hohl-Ebinger, J., Yoshita, M., Kopidakis, N., and Hao, X. (2021). Solar cell efficiency tables (version 57). *Progress in photovoltaics: research and applications*, 29(1):3–15.

Green, M. A., Ho-Baillie, A., and Snaith, H. J. (2014). The emergence of perovskite solar cells. *Nature photonics*, 8(7):506–514.

Horcas, I., Fernández, R., Gómez-Rodríguez, J. M., Colchero, J., Gómez-Herrero, J., and Baro, A. M. (2007). WSXM: A software for scanning probe microscopy and a tool for nanotechnology. *Review of Scientific Instruments*, 78(1):013705.

Im, J.-H., Jang, I.-H., Pellet, N., Grätzel, M., and Park, N.-G. (2014). Growth of ch3nh3pbi3 cuboids with controlled size for high-efficiency perovskite solar cells. *Nature nanotechnology*, 9(11):927–932.

Kardar, M., Parisi, G., and Zhang, Y.-C. (1986). Dynamic scaling of growing interfaces. *Physical Review Letters*, 56(9):889.

Kim, H.-S., Lee, C.-R., Im, J.-H., Lee, K.-B., Moehl, T., Marchioro, A., Moon, S.-J., Humphry-Baker, R., Yum, J.-H., Moser, J. E., et al. (2012). Lead iodide perovskite sensitized all-solid-state submicron thin film mesoscopic solar cell with efficiency exceeding 9%. *Scientific reports*, 2(1):1–7.

Kittel, C. and McEuen, P. (2018). *Introduction to solid state physics*. John Wiley & Sons.

Kojima, A., Teshima, K., Shirai, Y., and Miyasaka, T. (2009). Organometal halide perovskites as visible-light sensitizers for photovoltaic cells. *Journal of the american chemical society*, 131(17):6050–6051.

Kumar, G. R., Savariraj, A. D., Karthick, S., Selvam, S., Balamuralitharan, B., Kim, H.-J., Viswanathan, K. K., Vijaykumar, M., and Prabakar, K. (2016). Phase transition kinetics and surface binding states of methylammonium lead iodide perovskite. *Physical Chemistry Chemical Physics*, 18(10):7284–7292.

Li, J., Han, Z., Gu, Y., Yu, D., Liu, J., Hu, D., Xu, X., and Zeng, H. (2021). Perovskite single crystals: synthesis, optoelectronic properties, and application. *Advanced Functional Materials*, 31(11):2008684.

Nečas, D. and Klapetek, P. (2012). Gwyddion: an open-source software for SPM data analysis. *Central European Journal of Physics*, 10:181–188.

Parr, R. G. and Weitao, Y. (1995). *Density-Functional Theory of Atoms and Molecules*. Oxford University Press.

Parveen, S., Obaidulla, S. M., and Giri, P. (2020). Growth kinetics of hybrid perovskite thin films on different substrates at elevated temperature and its direct correlation with the microstructure and optical properties. *Applied Surface Science*, 530:147224.

Sinha, S., Sirota, E., Garoff, S., and Stanley, H. (1988). X-ray and neutron scattering from rough surfaces. *Physical Review B*, 38(4):2297.

Wang, S., Yousefi Amin, A. A., Wu, L., Cao, M., Zhang, Q., and Ameri, T. (2021). Perovskite nanocrystals: Synthesis, stability, and optoelectronic applications. *Small Structures*, 2(3):2000124.

Xiao, Z., Song, Z., and Yan, Y. (2019). From lead halide perovskites to lead-free metal halide perovskites and perovskite derivatives. *Advanced Materials*, 31(47):1803792.